CASL-U-2011-0242-001

Power uprates
and plant life extension

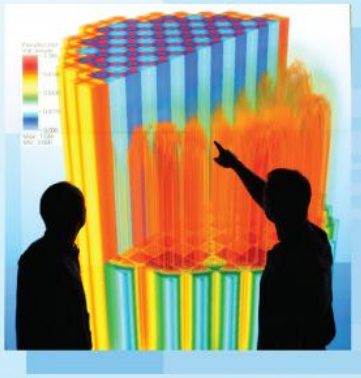

Engineering design
and analysis

Science-enabling
high performance
computing

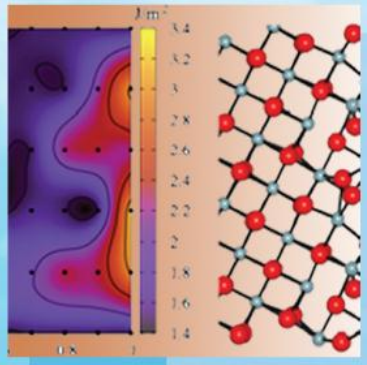

Fundamental science

Plant operational data

Consortium for Advanced Simulation of LWRs

L2:THM.P4.01

Rob Lowrie
LANL

Completed: 12/22/11

U.S. DEPARTMENT OF ENERGY | Nuclear Energy

LA-UR-11-07034

Approved for public release;
distribution is unlimited.

Title: Initial Assessment of Hydra-TH on Grid-to-Rod Fretting Problems (THM.CFD.P4.01)

Author(s):
Mark A. Christon
Jozsef Bakosi
Nathan Barnett
Marianne M. Francois
Robert B. Lowrie

Intended for: CASL L2 Milestone POR4

Los Alamos National Laboratory, an affirmative action/equal opportunity employer, is operated by the Los Alamos National Security, LLC for the National Nuclear Security Administration of the U.S. Department of Energy under contract DE-AC52-06NA25396. By acceptance of this article, the publisher recognizes that the U.S. Government retains a nonexclusive, royalty-free license to publish or reproduce the published form of this contribution, or to allow others to do so, for U.S. Government purposes. Los Alamos National Laboratory requests that the publisher identify this article as work performed under the auspices of the U.S. Department of Energy. Los Alamos National Laboratory strongly supports academic freedom and a researcher's right to publish; as an institution, however, the Laboratory does not endorse the viewpoint of a publication or guarantee its technical correctness.

Form 836 (7/06)

CASL-U-2011-0242-001

Initial Assessment of Hydra-TH on Grid-to-Rod Fretting Problems (L2 Milestone THM.CFD.P4.01)

Mark A. Christon, Jozsef Bakosi, Nathan Barnett,
Marianne Francois, and Rob Lowrie
Los Alamos National Laboratory
Los Alamos, NM 87544

With contributions from:
R. Pawlowski, J. Shadid, and T. Smith, Sandia National Laboratories

1 Executive Summary

This report describes the work carried out for completion of the Thermal Hydraulics Methods (THM) Level 2 Milestone THM.CFD.P4.01 for the Consortium for Advanced Simulation of Light Water Reactors (CASL). This milestone is primarily focused on the application of Hydra-TH to the grid-to-rod fretting (GTRF) problem using meshes provided by Sandia National Laboratories and used for their initial large-eddy simulations with the Drekar code.

This milestone was comprised of 5 sub-tasks that included: 1) Regeneration of the 5 GTRF meshes used by Sandia for their Drekar simulations [6], 2) initial calculations using the 5 GTRF meshes with symmetry conditions imposed along the edges of the 3×3 rod bundle, 3) repeat the calculations in task-2 using periodic conditions along the edges of the 3×3 rod bundle if the periodic conditions are available, 4) generate "spider" meshes using Hexpress/Hybrid for the GTRF configuration and perform demonstration calculations, and 5) produce representative power spectral density (PSD) forcing functions from force time-history data.

A series of computations on the GTRF meshes delivered from Sandia have been carried out using Hydra-TH and three different turbulence models: implicit large-eddy simulation (ILES), detached-eddy simulation (DES), and Spalart-Allmaras (SA). A preliminary investigation indicated that all calculations should be carried out to approximately $t = 1\ s$ in order to achieve a statistically stationary state for the three models. In general, the overall mesh quality is relatively poor for LES calculations with under-resolved boundary layers and rapid jumps in mesh resolution. In effect, the ILES and DES calculations are essentially very large-eddy simulation, or more simply "dirty LES".

A qualitative comparison between the velocity distributions computed by Elmahdi, et al. [2] show reasonable agreement in terms of the vortical structure and in-plane velocity magnitude despite the factor of 16 difference in mesh resolution (3M element mesh for Hydra-TH vs. the 48M element mesh reported by Elmahdi, et al.) However, pressure drop comparisons between the Hydra-TH, Drekar and the CCM+ results of Elmahdi, et al. leave a number of unanswered questions. The presence of relatively strong vortical motion at the outflow boundary suggests that this boundary is too close to the spacer, or that alternative boundary conditions are required for this domain.

The results presented for the ILES, DES and Spalart-Allmaras turbulence models in §3.2.1 – 3.2.3 indicates a number of differences in the computed results. This is not surprising

CASL-U-2011-0242-001

given the nature of turbulence and the approaches to turbulence modeling. Despite using a time-accurate URANS approach with Spalart-Allmaras, the time-history force data suggest that this approach may not be a viable approach for GTRF calculations where the mean and RMS forces are of interest. However further studies with refined meshes and better boundary layer mesh grading are required to make a definitive statement. In addition, it may be worthwhile to investigate some level of turbulent statistics rather than only considering mean and RMS values of forces. In terms of design processes, it is anticipated that there are a number of loading and heat transfer metrics that would be useful in determining the "best" turbulence model for GTRF and ultimately an optimal spacer design. However, these metrics are not currently available, and a discussion of this topic is beyond the scope of this report.

In addition to the primary tasks for the milestones, a series of important steps were carried out as supporting work. This includes the scaling of the HDF5-based Exodus-II library to 1.8 billion cells. In addition, the Hydra-TH team has worked closely with Kitware to debug distance/parallel visualization between ORNL and LANL using the Jaguar platform. In addition, we have worked with Numeca on the integration of the Exodus-II, netcfd4, and HDF5 libraries into Hexpress/Hybrid. We are beginning a more serious use and evaluation of Hexpress/Hybrid for CASL-centric THM problems.

As we move forward with Hydra-TH, we are planning a series of additional steps relevant to the GTRF problem. These steps will include conducting a more detailed scaling study on Jaguar using meshes up to ≈ 1 billion elements, implementation of the WALE model, assessment of turbulence statistics for the ILES, DES and WALE model, and use of refined hybrid "Spider" meshes.

2 Introduction

The grid-to-rod fretting (GTRF) problem in pressurized water reactors is a flow-induced vibration problem that results in wear and failure of the rods in nuclear fuel assemblies. As pointed out in Elmahdi, et al. [2], to date, it has not been possible to completely characterize the flow-induced fluid-structure interaction (FSI) problem for the GTRF problem. Indeed, given the incompressible nature of the coolant, the relatively high Reynolds number, and the flexible character of the fuel rods and spacers, the FSI problem at the reactor core scale is daunting.

This work represents an initial evaluation of several turbulence models for a representative 3×3 rod bundle with a single spacer. Hydra-TH is used to compute the time-accurate and fully three-dimensional flow field for the 3×3 rod bundle. Force time-history data suitable for calculation of the dynamical response of the rod is computed and examined on the fuel-rod and spacer. From this data, we extract the average and root-mean-square (RMS) lateral forces on the central fuel rod in the bundle and the spacer.

In the ensuing discussion, the generation and assessment of the 5 GTRF meshes (Task-1) is presented in §3.1. The initial flow computations using the ILES, DES and Spalart-Allmaras models (Task-2) are summarized in §3.2. At the time of this writing, the periodic boundary conditions are not complete, and no calculations have been performed for the conditional Task-3. In §3.3, we briefly summarize the status of efforts with Hexpress/Hybrid (Task-4). Task-5, the generation of force PSD's for the 3×3 GTRF configuration is discussed with the results presented in §3.2. Section §4 summarizes the results from the initial Hydra-TH GTRF calculations.

3 Milestone Accomplishments

3.1 Mesh Generation & Assessment (Task-1)

Sandia National Laboratories provided a total of 8 Cubit journal files for the 5 meshes reported in Table 1 of the level 3 milestone report THM.CFD.P2.01 [6]. Of the 8 journal files, we were able to identify the 5 corresponding to the 672k, 1M, 3M, 6M and 12M element meshes in Table 1. The remaining 3 journal files appeared to include the solid rod and spacer with the fluid domain. All of the journal files contained a header showing they were generated with Cubit version 13, build 45777.

Cubit version 13, build 46397, was exercised on both Linux and MacOS machines with mixed results. Using MacOS, all of the journal files caused Cubit to crash. Using Linux, we were able to successfully generate meshes from the 672k, 1M, 3M and 6M journal files. Unfortunately, the 12M journal file also caused Cubit to crash on Linux. All of the journal files produced what appear to be serious warnings about negative Jacobians for hex elements indicating problems with the mesh quality. Sandia National Laboratories provided the Exodus-II file for the 12M element mesh by secure file transfer.

All of the generated Exodus-II files contained 9 side-sets corresponding to the inlet, outlet, rod and spacer surfaces, and the exterior regions of the 3×3 rod array. We were able to easily use the side-sets with Hydra-TH for the specification of all necessary boundary conditions as outlined in §3.2. However, we note that the 12M mesh was translated in the z coordinate direction by 0.2127 m relative to the other four meshes. Where necessary, we made the necessary adjustments in our post-processing of results to account for the relative translation.

Initial inspection of all 5 grids revealed a lack of mesh grading consistent with boundary layers on the rod and spacer surfaces. Figure 1 shows that the transitions between the mesh blocks upstream and downstream of the spacer are quite abrupt with a relatively large jump in mesh resolution from the "hex-tet" mesh around the spacer to the all hex regions. For LES computations, abrupt transitions from the spacer region, where small eddies are generated by the spacer geometry, to the downstream section will result in aliasing to longer-wavelengths. This is particularly unfortunate for LES computations since this will result in an upscale aliasing of energy from the short-wavelength eddies generated by the spacer to the eddies that the coarser downstream mesh can resolve. Needless to say, this is an undesirable artifact that can't be avoided with the meshes provided for the GTRF.

In addition, to the qualitative assessment of the meshes, a more quantitative assessment was based on the minimum/maximum y^+ at the spacer and rod surfaces. For LES, it is typical to require $y^+ \approx 1$, with a sufficiently smooth transition to the free-stream mesh. For the DES and Spalart-Allmaras models, it is typical to expect that $y^+ \leq 3$. Figure 2 shows the y^+ distribution on the spacer and rod surfaces for the 3M mesh. Although the minimum y^+ is adequate, the large variations across the surface is problematic for any wall treatment, and will perturb the wall shear significantly – particularly where $O(10)$ jumps occur between adjacent surface elements. Given the non-monotone behavior of the y^+, and the local roughness, no attempt was made to use the RNG $k - \epsilon$ model with wall functions. In addition, it is anticipated that the lack of boundary-layer meshing and control of the y^+ at the wall may not yield regular convergence metrics in the forces on the rod and spacer surfaces. We also note that the minimum y^+ occurs only in small regions on the spacer cut-outs for all the meshes, while on the rod and spacer surfaces $20 \leq y^+ \leq 60$, resulting in a very poor quality LES mesh – at least in terms of boundary layer resolution.

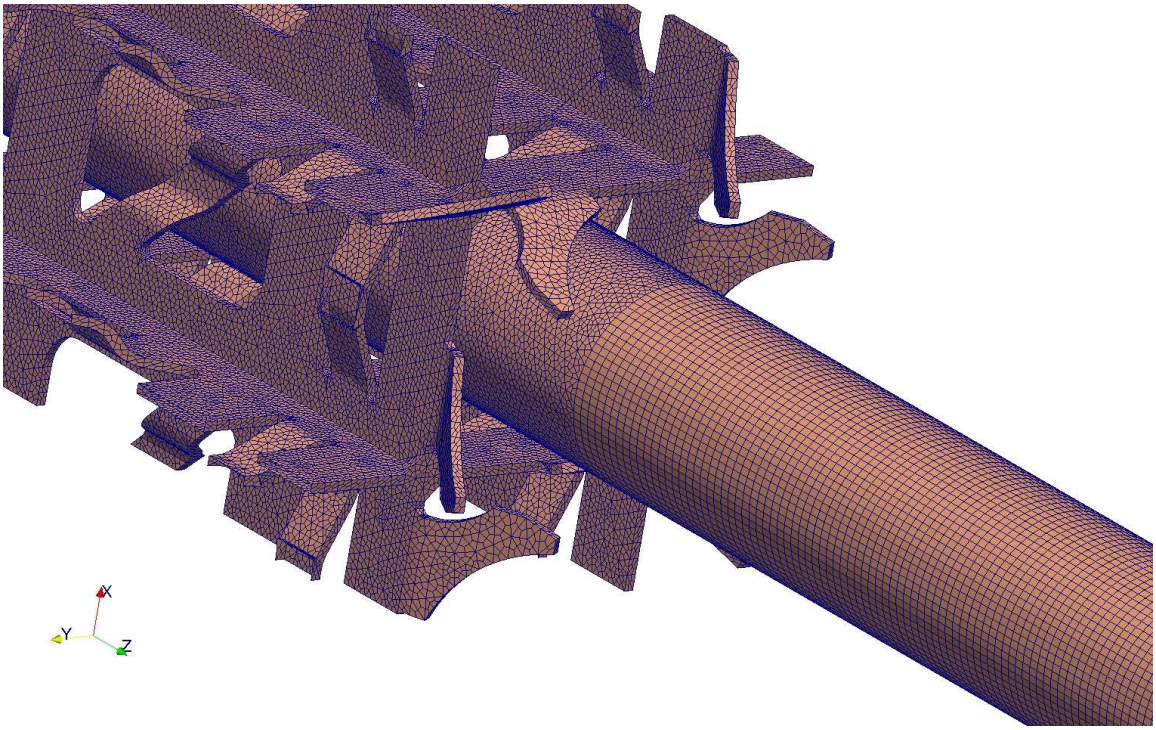

(a) Mesh spacing on center rod and spacer surfaces for the 3M mesh.

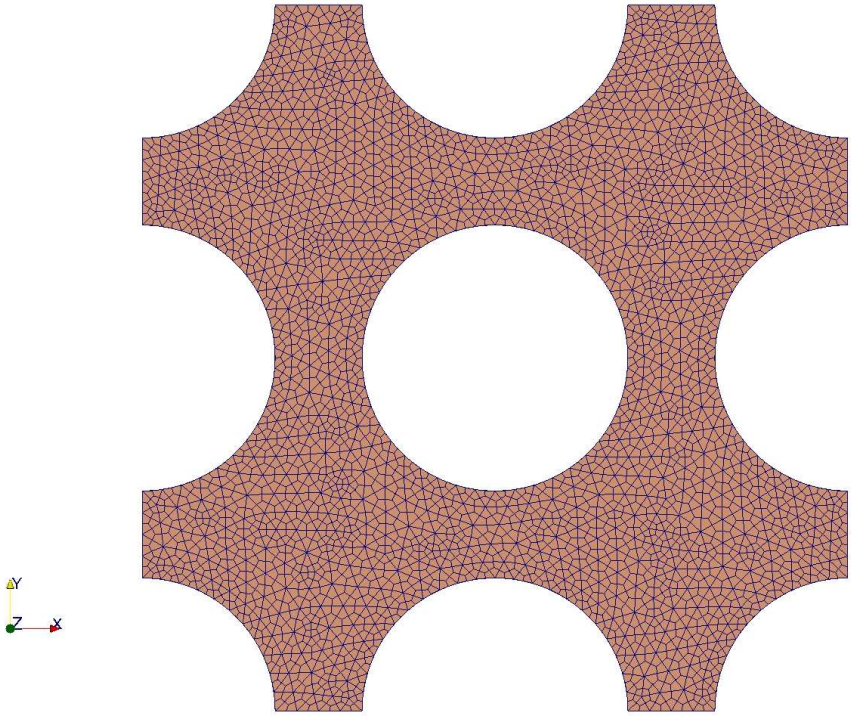

(b) Cross-section view of the mesh in the inlet region for the 3M mesh.

Figure 1: Element distribution for the 3M mesh.

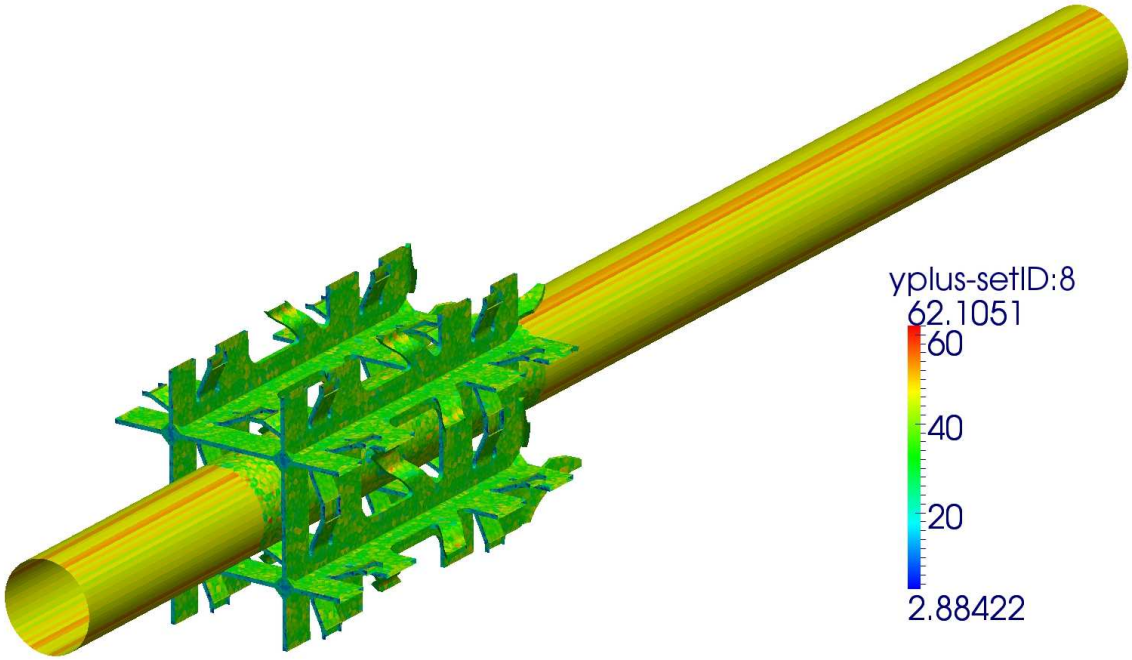

Figure 2: y^+ distribution on the center rod and spacer surfaces for the 3M element mesh.

Mesh	No. of Elements	y^+_{min}	y^+_{max}
672k	671,572	2.7388	86.0984
1M	1,049,228	3.4053	61.3910
3M	2,663,920	2.8842	62.1051
6M	5,832,718	0.9624	55.6384
12M	12,522,644	0.7452	45.1667

Table 1: GTRF meshes used for with ILES, DES and Spalart-Allmaras models with the associated min/max $y+$ values for the rod and spacer surfaces where no-slip/no-penetration boundary conditions are imposed.

3.2 Initial Flow Calculations (Task-2)

The flow conditions for the 3×3 GTRF follow those used by Elmahdi, et al. [2] and Shadid, et al. [6]. The flow domain in the meshes that were provided by Sandia, was only 17.86 diameters long compared to the approximately 32 diameter long domain used by Elmahdi, et al.

For the calculations reported here, the working fluid is water at a temperature of 394.2 K, a density of 942.0 kg/m^3, and a dynamic viscosity of 2.32×10^{-4} $kg/m/s$. The inlet velocity is prescribed as $\mathbf{v} = (0, 0, 5)$ m/s. This corresponds to a Reynolds number, based on the rod diameter, of $Re_D = 1.93 \times 10^5$, while the Reynolds number based on the hydraulic diameter is $Re_{D_h} = 4.01 \times 10^5$. The hydraulic diameter is defined as $D_h = 4A_{flow}/P_{wet}$. No-slip, no-penetration conditions are prescribed at the rod and spacer surfaces. At the outlet, the hydrostatic pressure is specified to be $p_h = 0.0$ in conjunction with a zero shear stress condition. For the first set of calculations, no-penetration conditions with in-plane slip were applied at the subchannel boundaries as shown in Figure 3.

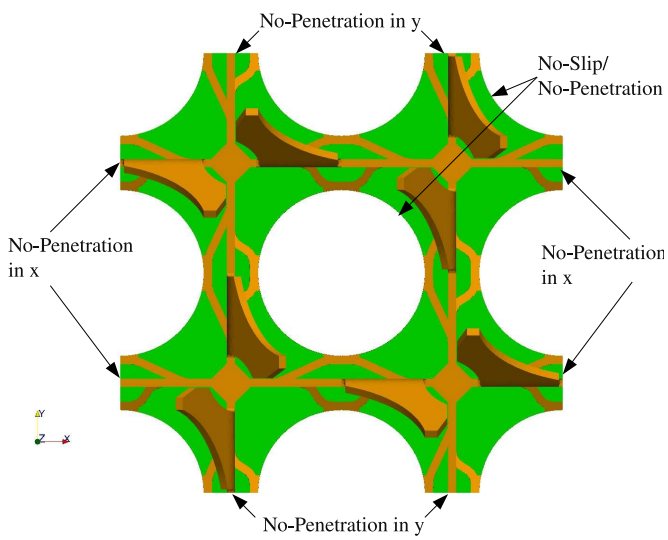

Figure 3: Boundary conditions on rod and spacer surfaces, and subchannel boundaries.

Each calculation was heavily instrumented to provide global, surface and point time-history data that included kinetic energy, RMS divergence, forces and tractions on the rod and spacer surfaces, and pointwise values of velocity and pressure. Surface forces are computed by integrating either tractions or pressures over the given surface. The pointwise data was sampled at the element-centroid closest to the time-history locations shown in Table 2. These locations were selected based on the results presented in Figure 4 of [6] and positioned along the central rod downstream of the spacer.

For the suite of 5 meshes, three turbulence models were exercised: a) ILES, b) DES, and c) Spalart-Allmaras. Details on these models may be found in the Hydra-TH Theory manual [1]. All calculations were performed in a time-accurate way using the neutrally-dissipative second-order trapezoidal rule time-integrator for a duration of 1 s of physical time. A fixed CFL condition was used for all calculations in conjunction with implicit time-weighting on the advective and diffusive terms.

Before presenting the results for the 3 turbulence models, we address the question of the duration of the flow simulations. A physical time of 1 s was selected based on prelimi-

Point	Location
p1	(4.7500E-3, 0.0000, 0.0848)
p2	(4.7500E-3, 0.0000, 0.0978)
p3	(4.7500E-3, 0.0000, 0.1176)
p4	(4.7500E-3, 0.0000, 0.1415)
p5	(4.7500E-3, 0.0000, 0.1676)

Table 2: Time-history locations for pointwise velocity and pressure measurements. (For the 12M mesh, all of the time-history locations were translated by 0.2127 m to account for the translation in the mesh location relative to the other 4 meshes.)

nary calculations with the 672k and 1M element meshes that indicated the ILES and DES calculations had achieved a statistically stationary state.

Figure 4 shows the time-history data for ILES for the global kinetic energy, pressure at the 5 locations shown in Table 2, and the spacer and rod forces in the cross-stream direction for mesh 1M. Here, the global kinetic energy is defined as $KE = \int_\Omega \rho \mathbf{v} \cdot \mathbf{v}/2 d\Omega$. Although the kinetic energy and pressure appear to reach a stationary state very quickly, the startup transient is still evident in the lateral forces up to approximately 0.15 s. For this reason, mean values and turbulent statistics are collected after 0.2 s. A stationary state is clearly evident after approximately 0.2 s where there is a fluctuation around a clearly defined mean for all of the time-history data. We have tested the sensitivity of the mean quantities by performing averages for $0.2 \leq t \leq 0.6$ and comparing to the average for $0.2 \leq t \leq 1.0$. Although this is not a rigorous assessment, the mean forces differed by less than 0.5% for the two averages indicating that 1 s was a reasonable duration for these preliminary calculations.

In addition to the time averages, we estimated the number of flow transits for the 1 s duration calculations. Given the 5 m/s inlet velocity, a 1 s time scale corresponds to approximately 30 flow transits through the length of the computational domain. For the spacer region, this corresponds to approximately 131 flow transits.

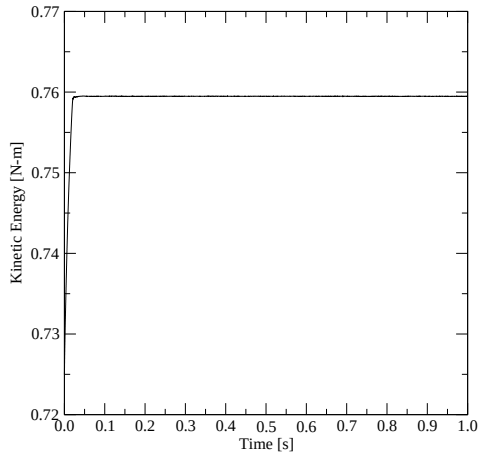

(a) Global kinetic energy time history.

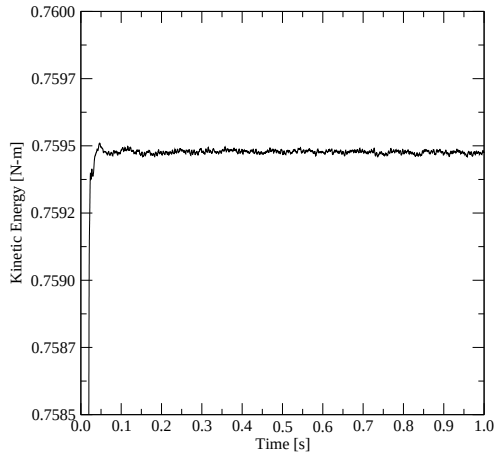

(b) Zoom-in of global kinetic energy time history.

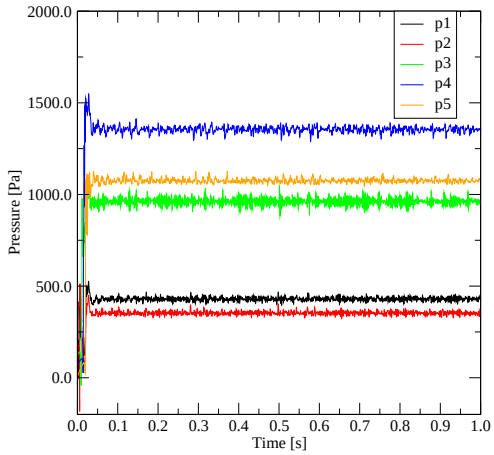

(c) Pressure time histories.

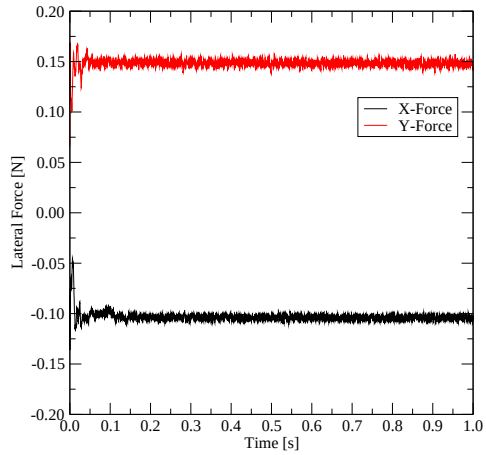

(d) Lateral force time histories on central rod.

Figure 4: ILES time-history data for mesh 1M showing (a) global kinetic energy, (b) zoom-in of kinetic energy, (c) pressure time histories, and (d) lateral force time histories on the central rod.

3.2.1 ILES Results

The ILES calculations were carried out using a fixed $CFL = 4$ condition for all meshes. The asymptotic time-step for each mesh is shown in Table 3. The variability in time-step size with respect to the mesh size reveals that the underlying meshing strategy did not provide any form of uniform refinement as the time-step size is oscillatory with respect to mesh resolution. Surprisingly, the 672k mesh had the smallest time-step size at $CFL = 4$ due to a relatively large velocity that encountered a relatively small element size in the flow domain. We did not attempt to identify mesh pathologies associated with this behavior, but note in passing that this makes a systematic convergence study problematic.

Mesh	CFL	Avg. Time Step
672k	4	1.58E-5
1M	4	2.40E-5
3M	4	3.36E-5
6M	4	1.86E-5
12M	4	2.33E-5

Table 3: Average time-step based on a fixed-CFL number used for the ILES calculations.

Figure 5 shows the in-plane velocity and pressure distribution at two locations downstream of the spacer. The locations match those used in Elmahdi, et al. [2]. At both locations, the pressure distribution reveals relatively strong vortical cores in the subchannels surrounding the central rod. In addition, multiple secondary and some tertiary vortical structures are readily visible in the subchannels. A maximum velocity magnitude of 2.982 m/s at $z = 0.1135$ m, and 2.485 m/s are calculated by Hydra-TH on the 3M mesh. In comparison to the results presented in Elmahdi, et al., where a mesh with 48 million elements was used, peak velocities of 3.5794 m/s and 3.2844m/s at the two planes were reported respectively. Qualitatively, the secondary vortices in the rod gaps are similar, although the Hydra-TH results suggest stronger vortical structures than evident in the CCM+ results presented by Elmahdi, et al.

The planar velocity distributions in Figure 5, suggest the presence of strong helical structures that propagate downstream from the mixing vanes on the spacer. This is shown explicitly in the instantaneous helicity isosurfaces in Figure 6. Here, the correlation between the streamwise velocity component and the vorticity is shown in pairs of co-rotating eddies whose directions are aligned in the primary flow direction. In addition, the vortical structures tend to wrap around the central rod revealing an overall circumferential swirl in the flow as shown in Figure 5(b).

The kinetic energy time histories and line plots of the pressure along the surface of the central rod are shown in Figure 7. We attempted to use the exact same line as reported in Figure 3 of Shadid, et al. [6], i.e, from (4.75E-3,0.0,0.0) to (4.75E-3,0.0,0.1697). However, in the meshes supplied by Sandia National Laboratories, this line intersects the spacer at two points along the central rod. For this reason, the line plots reported here are from (3.3588E-3,3.3588E-3,0.0) to (3.3588E-3,3.3588E-3,0.1697) which avoids any intersections with the spacer. The kinetic energy and maximum pressure both reveal a non-monotonic behavior relative to the mesh resolution, i.e., the 1M mesh shows a lower average kinetic energy than the 672k mesh. This suggests that the 672k mesh is simply too coarse, and as already mentioned, too rough, to draw any meaningful conclusions. Omitting the 672k results, both the maximum pressure and average kinetic energy tend to increase with increasing

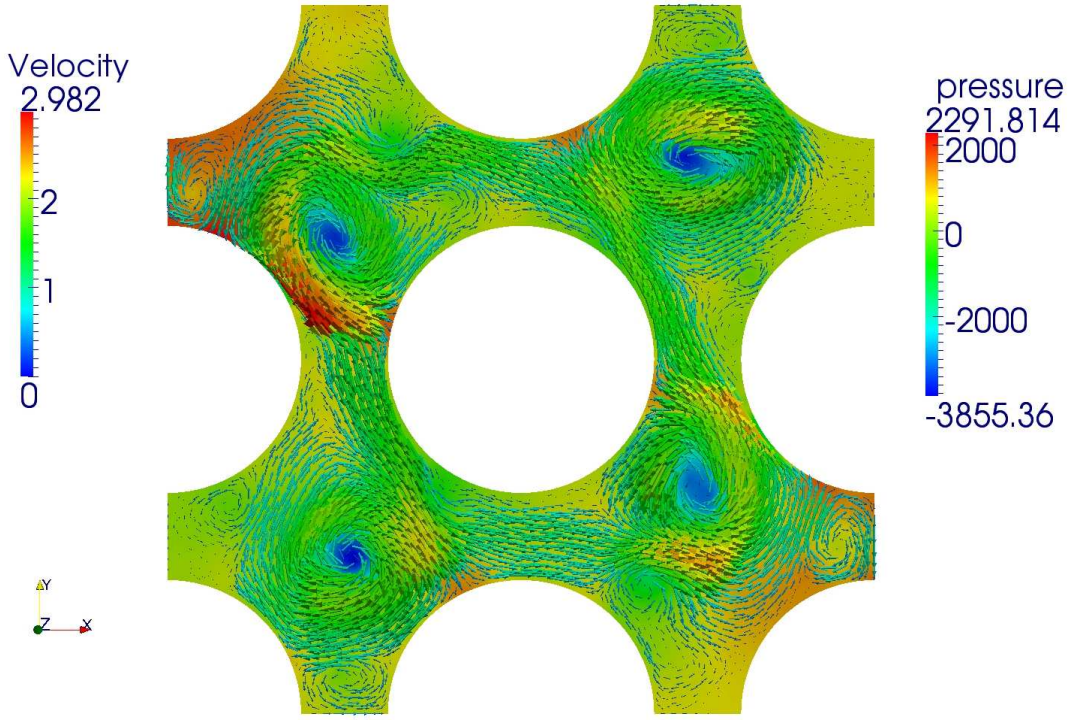

(a) Snapshot of in-plane velocity at $z = 0.1135\ m$

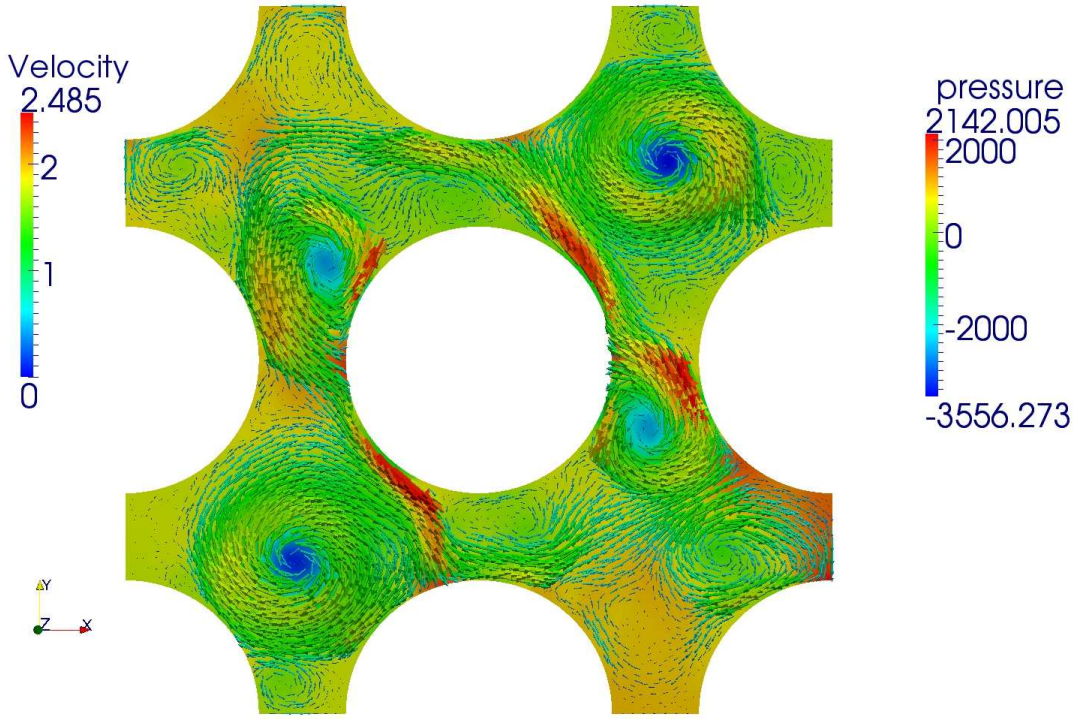

(b) Snapshot of in-plane velocity at $z = 0.1466\ m$.

Figure 5: Snapshots of instantaneous velocity and pressure on cutplanes for the 3M mesh at $t = 1\ s$ using the ILES model.

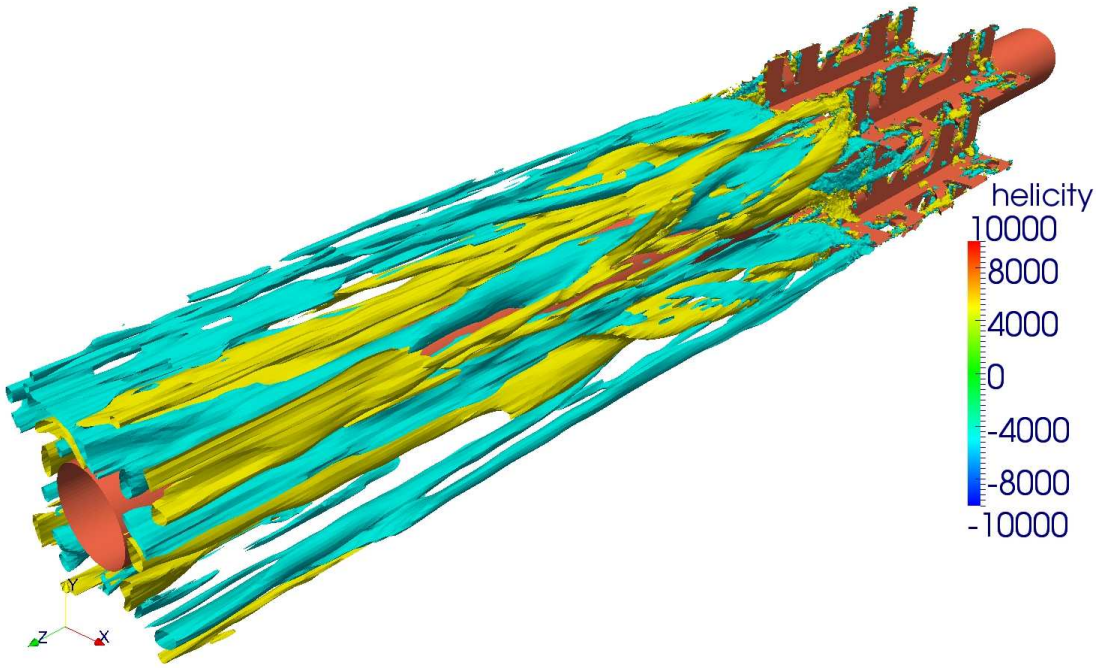

(a) Snaphost of helicity isosurfaces.

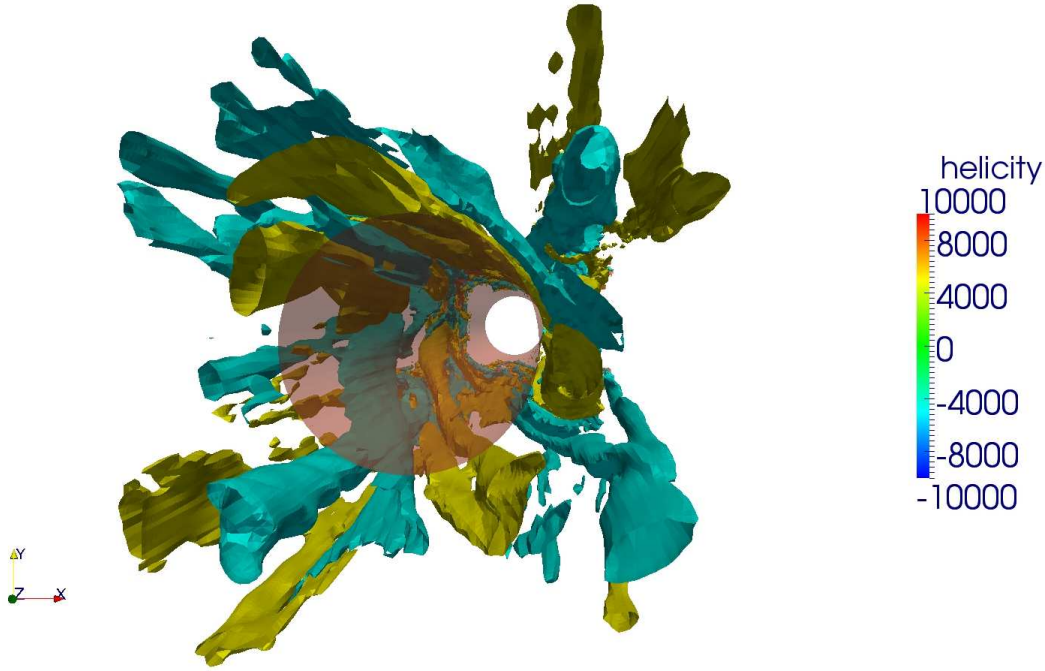

(b) Snaphost of helicity isosurfaces.

Figure 6: Instantaneous isosurfaces of helicity ($\mathbf{v} \cdot \omega$) for the 3M mesh at $t = 1\ s$ using the ILES model. Isosurface values $\pm 5000\ m/s^2$.

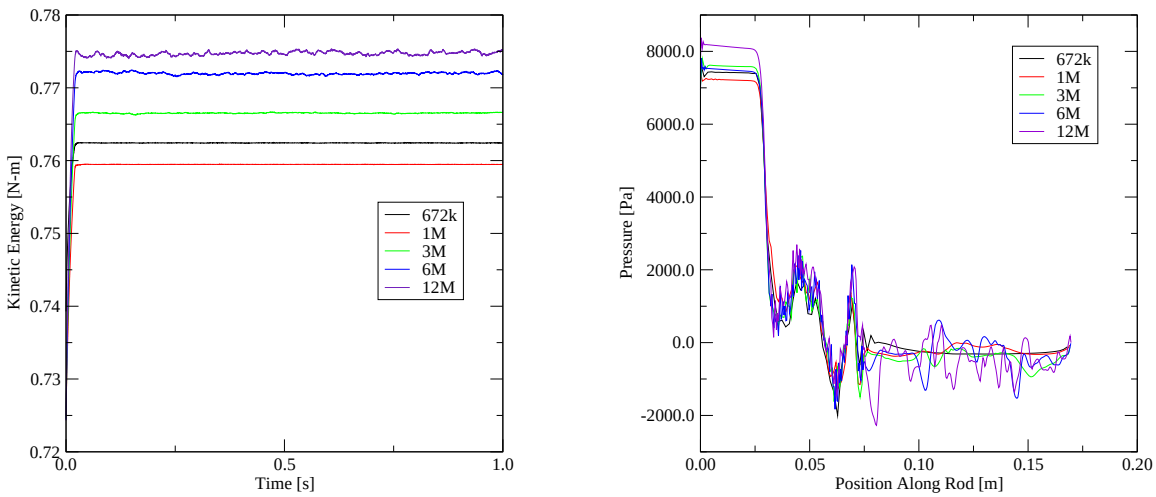

(a) Kinetic energy time history.

(b) Pressure line plots.

Figure 7: Global kinetic energy time histories, and instantaneous pressure line plots for the 5 meshes using the ILES model.

mesh resolution. See the discussion in §3.2.4. In addition, the finer meshes exhibit larger excursions in kinetic energy from the average. The variation in pressure downstream of the spacer is evident in Figure 7(b), and indicates that the line used for the pressure output intersected the longitudinal vortical structures.

The cross-stream (lateral) forces on the rod and spacer are shown in Figure 8. Here, we compare the total integrated force on the central rod and spacer to the forces due to the pressure and the shear for the 3M mesh. Again, stationary behavior in all of the time-history forces is evident for $t > 0.2\ s$. For the central rod, the loads are dominated by the pressure. Shear forces on the rod and spacer in the lateral direction are negligible relative to the pressure loads, while the streamwise pressure forces on the rod are zero. In contrast, the streamwise pressure loads on the spacer are an order of magnitude larger than the pressure loads on the cylinder, reinforcing the idea that the spacer induces all the pressure drop. This is also shown in Figure 7(b).

Spectral data for the x and y components of the total forces on the rod surface are plotted in Figure 9 for the 3M ILES calculations. Both an FFT and Welch's PSD were performed on time histories in the range $0.2s < t < 1.0s$. Welch's PSD [7] of the discrete force time history, $f(t_k)$, is computed as

$$F(\omega_k) = \left(\frac{1}{M} \sum_{m=0}^{M-1} \left| \mathrm{DFT}_k \left[f(t_m) \right] \right|^2 \right)^{1/2}, \tag{1}$$

where m denotes the block index within the smoothing block of size M, and DFT stands for discrete Fourier transform. The data in Figure 9 was obtained with $M = 20$, which is a useful compromise between smoothing and retaining large-amplitude frequency spikes.

Using the force time-history data, we compute the average and RMS forces on the rod and spacer in the cross-flow directions. Table 4 shows the average and RMS forces in the

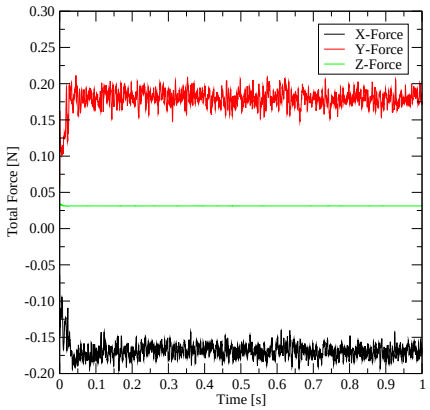

(a) Total force on the central rod.

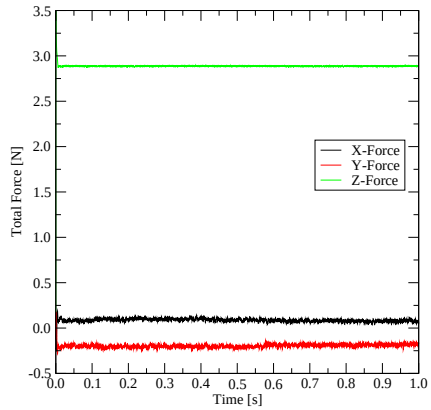

(b) Total force on the spacer.

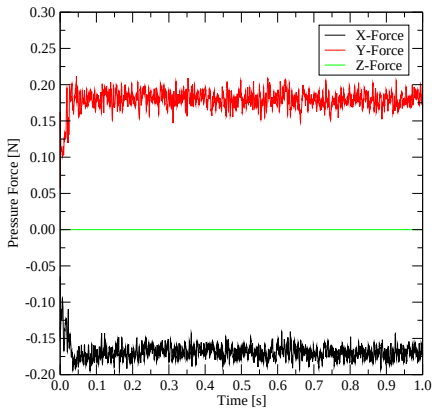

(c) Pressure force on the central rod.

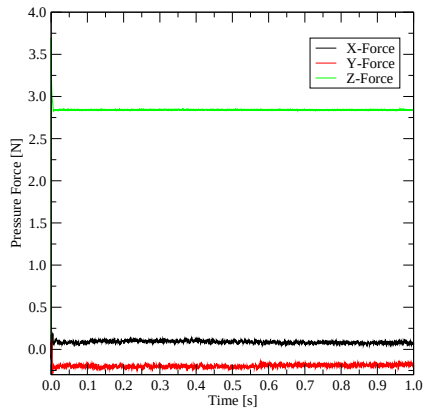

(d) Pressure force on the spacer.

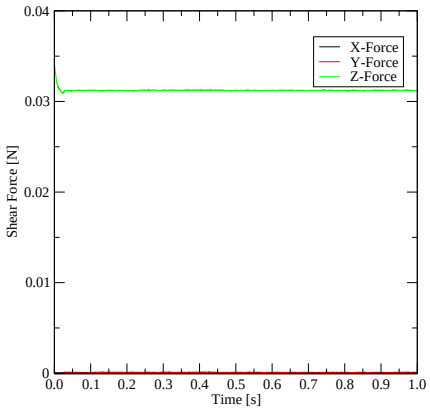

(e) Shear force on the central rod.

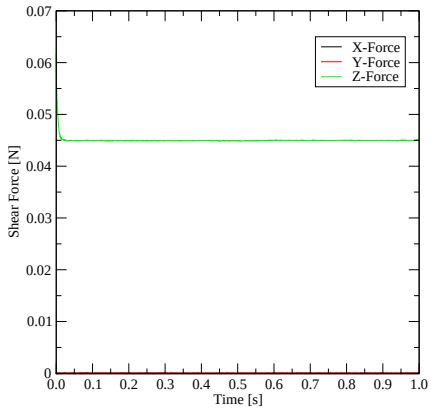

(f) Shear force on the spacer.

Figure 8: Total, pressure, and shear force time histories on the central rod and spacer for the 3M mesh using the ILES model.

x and y-direction for the 5 meshes. Due to the asymmetric nature of the spacer and the resulting effects on the flow, the average and RMS forces are not equal in the x and y-directions. This effect was reported in Elmahdi, et al. [2]. The forces are seen to increase with mesh resolution. As a basis for comparison, the force values reported here correspond approximately to the integrated forces over the first 7 rod segments reported by Elmahdi, et al. Summing the forces in Table 7 of Elmahdi, et al. and accounting for the fact that our flow domain covers only 67% of the 7th rod segment, the RMS forces from Elmahdi, et al. are estimated to be (0.1082, 0.1407) N acting in the x and y-directions respectively. For the 12M mesh, the RMS forces are under-predicted by 62% in x, and by 67% in y relative to Elmahdi, et al.. The under-prediction is not surprising given the relatively coarse and rough boundary layer meshes. Unfortunately, the rod surface was not broken into segments corresponding to those used by Elmahdi, et al., so more direct comparisons were not possible.

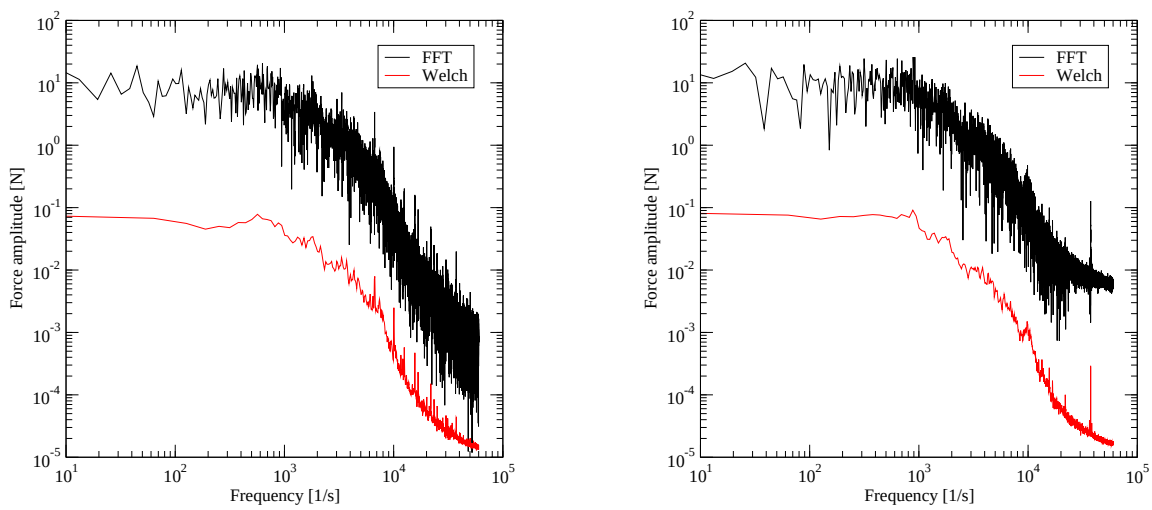

(a) FFT and Welch's PSD of the x-force.

(b) FFT and Welch's PSD of the y-force.

Figure 9: FFT and Welch's PSD of the force in the x and y directions on the central rod surface for the 3M mesh from the ILES calculations.

	Rod Surface				Spacer Surface			
	X-Force		Y-Force		X-Force		Y-Force	
Mesh	Avg.	RMS	Avg.	RMS	Avg.	RMS	Avg.	RMS
672k	-0.1258	1.5384E-3	0.0884	1.8006E-3	0.0310	7.3843E-3	-0.2145	7.6515E-3
1M	-0.1040	1.8989E-3	0.1484	2.8370E-3	0.0632	7.6399E-3	-0.1552	6.5946E-3
3M	-0.1688	7.9235E-3	0.1780	9.6089E-3	0.0865	1.5824E-2	-0.1943	1.6256E-2
6M	-0.1416	2.3888E-2	0.1630	3.0144E-2	0.1166	1.9478E-2	-0.1882	2.0098E-2
12M	-0.08034	4.1150E-2	0.0740	4.8622E-2	0.0226	4.7954E-2	-0.1782	5.0801E-2

Table 4: Time averaged and RMS lateral forces on the rod and spacer surface for the ILES model.

3.2.2 DES Results

The DES calculations were also carried out using a fixed $CFL = 4$ condition for all meshes. The asymptotic time-step for each mesh is shown in Table 5. Relative to the ILES calculations, the time-steps are comparable, and also show the oscillatory behavior relative to mesh resolution. At this time, the 6M and 12M results are only partially complete, and not included here.

Mesh	CFL	Avg. Time Step
672k	4	1.63E-5
1M	4	2.32E-5
3M	4	3.35E-5
6M	4	1.97E-5
12M	4	2.34E-5

Table 5: Average time-step based on a fixed-CFL number used for the DES calculations.

Figure 10 shows the in-plane velocity and pressure distribution at two locations downstream of the spacer. Similar to the ILES results, the pressure distribution reveals relatively strong vortical structures in the subchannels surrounding the central rod. In addition, multiple secondary and some tertiary vortical structures are readily visible in the subchannels. A maximum velocity magnitude of 2.933 m/s at $z = 0.1135$ m, and 2.546 m/s are calculated by Hydra-TH on the 3M mesh. These values are just slightly higher than the in-plane velocities predicted using the ILES model. As with the ILES calculations, the secondary vortices in the rod gaps are qualitatively similar to the structured reported by Elmahdi, et al [2].

Figure 11 shows snapshots of instantaneous helicity isosurfaces. Similar to the ILES results, there are small structures generated on the surface of the spacer, with large coherent and persistent helical structures in the wake of the mixing vanes. The overall structure of the wake is very similar to the ILES results. However, the DES model appears to produce somewhat sharper helical structures in the downstream region. At this time, we have not performed any statistical analyses to quantify the differences in terms of more fundamental turbulence quantities. However, the ILES and DES results indicate qualitatively that the vortices generated by the mixing vanes are correlated with the flow velocity, and the strength of the helical structures is such that the longitudinal vortices propagate a considerable distance downstream.

The kinetic energy time histories and line plots of the pressure along the surface of the central rod are shown in Figure 12 for the 672k and 3M meshes. Here, we use the same line coordinates as presented above for the ILES results.

The cross-stream forces on the rod and spacer are shown in Figure 13. Similar to the ILES results, the forces on the rod and spacer are dominated by pressure. The shear forces on the central rod are negligibly small relative to the pressure forces. In contrast to the ILES results, the DES force time-histories show somewhat muted oscillations around a mean after achieving a stationary state. However, the mean forces are close to those computed with the ILES. As the DES results are still incomplete, a more complete comparison is not possible.

Figure 14 shows the FFT and Welch's PSD for the x and y-forces on the rod. A smoothing window of size $M = 20$ was used for the Welch PSDs. Making use of the force time-history data for the rod and spacer, the average and RMS forces on the rod and spacer in the cross-flow directions are reported in Table 6. The average forces are comparable to those calculated with the ILES model. This indicates that the lowest-order statistical turbulence measures

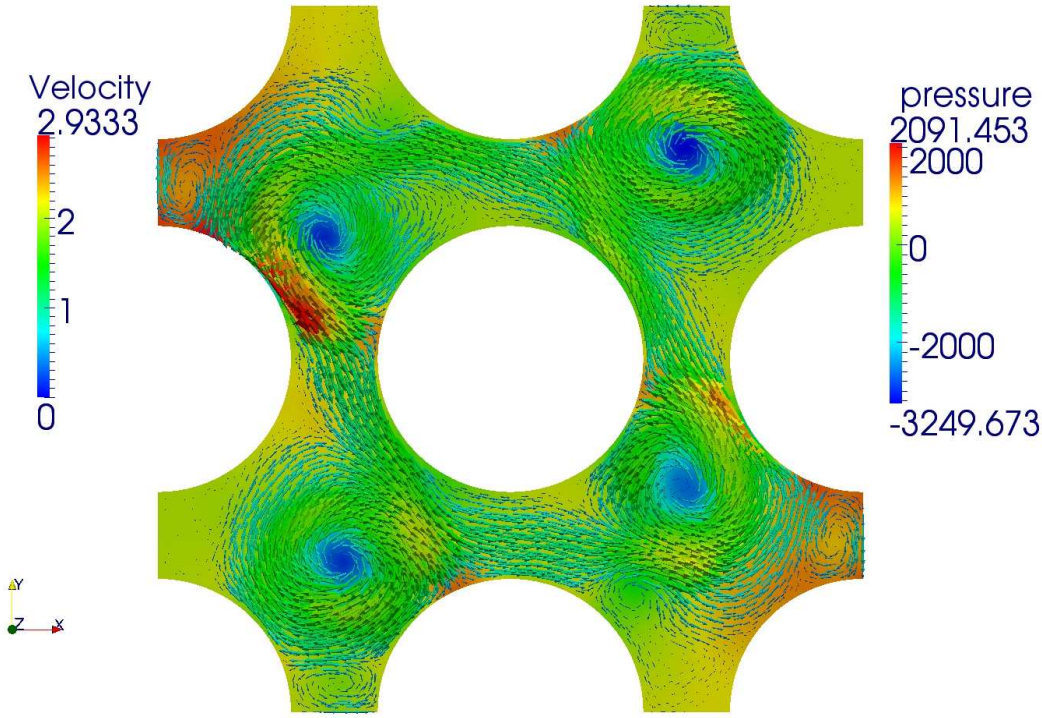

(a) Snapshot of in-plane velocity at $z = 0.1135\ m$

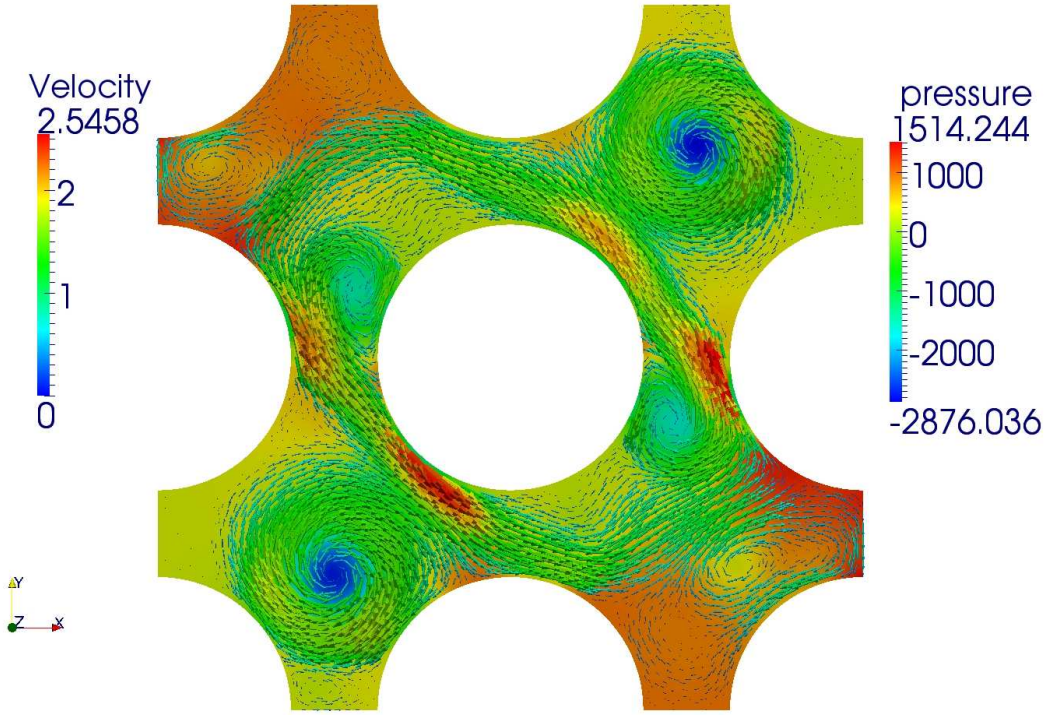

(b) Snapshot of in-plane velocity at $z = 0.1466\ m$.

Figure 10: Snapshots of instantaneous velocity and pressure on cutplanes for the 3M mesh at $t = 1\ s$ using the DES model.

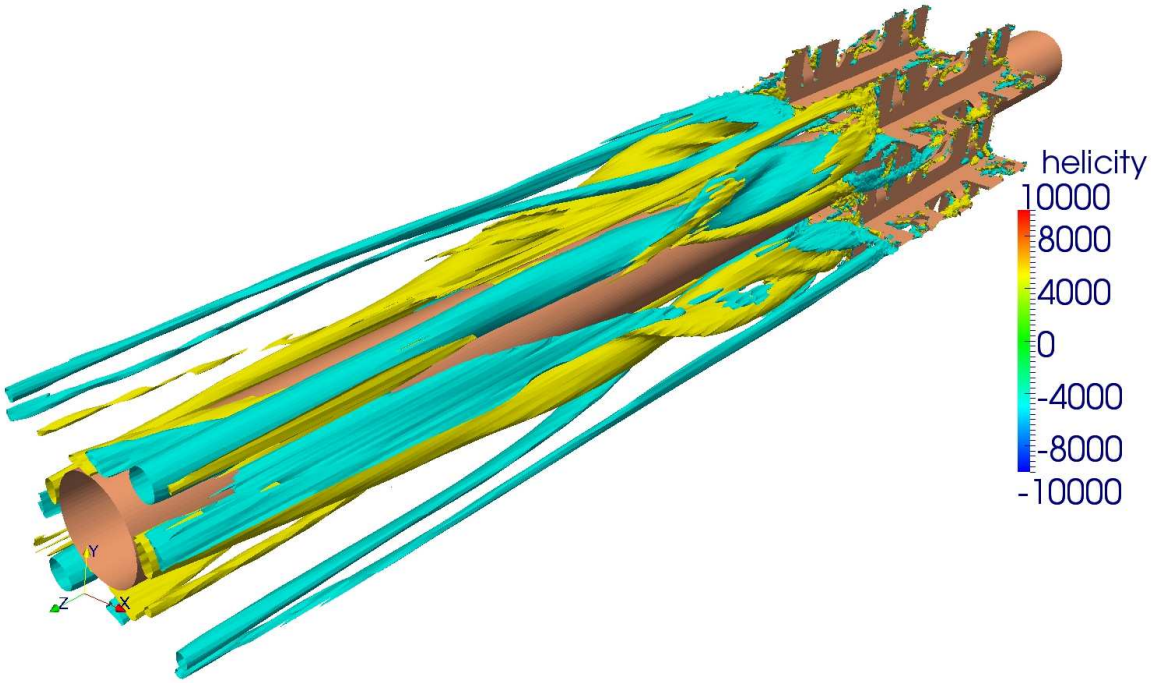

(a) Snaphost of helicity isosurfaces.

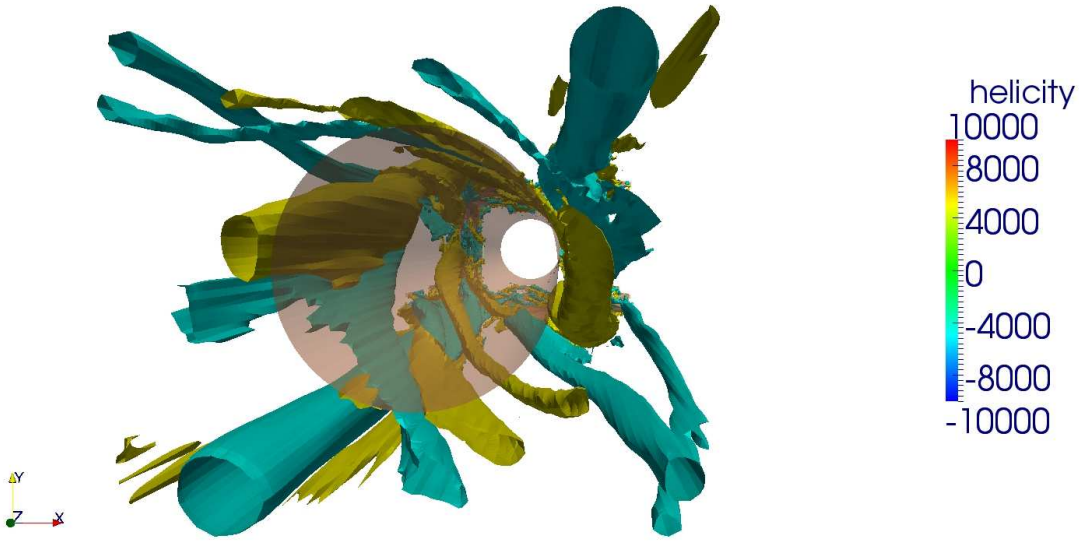

(b) Snaphost of helicity isosurfaces.

Figure 11: Instantaneous isosurfaces of helicity ($\mathbf{v} \cdot \omega$) for the 3M mesh at $t = 1\ s$ using the DES model. Isosurface values $\pm 5000\ m/s^2$.

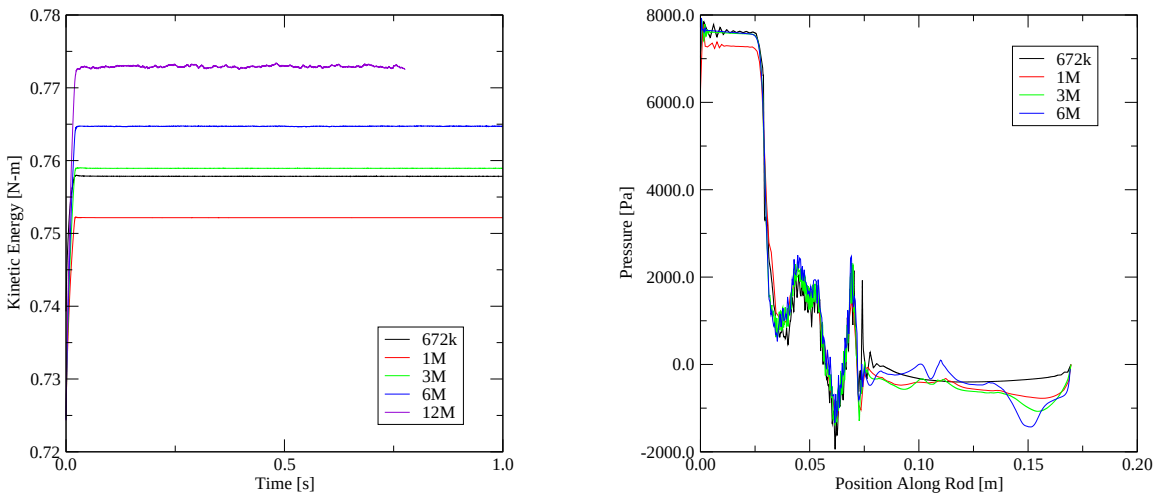

(a) Kinetic energy time history.

(b) Pressure line plots.

Figure 12: Global kinetic energy time histories, and instantaneous pressure line plots using the DES model.

(i.e., mean quantities), can accurately be computed with DES which may be relatively less expensive than ILES with fully-resolved boundary layers. Further studies with meshes that include graded boundary layer regions and smooth transitions from the spacer region to the downstream regions are necessary to assess the differences in the models to the degree necessary.

	Rod Surface				Spacer Surface			
	X-Force		Y-Force		X-Force		Y-Force	
Mesh	Avg.	RMS	Avg.	RMS	Avg.	RMS	Avg.	RMS
672k	-0.1446	6.3005E-4	0.1062	1.1284E-3	0.0456	4.0489E-3	-0.1903	3.1390E-3
1M	-0.0860	2.9517E-4	0.1927	3.1298E-4	0.0977	1.0705E-2	-0.0824	1.0203E-2
3M	-0.1531	1.5248E-3	0.1831	1.7860E-3	0.1131	4.1886E-3	-0.1863	4.0268E-3
6M	-0.1772	3.7145E-3	0.1778	4.7941E-3	0.0417	6.7342E-3	-0.0744	5.7780E-3
12M	-0.0323	2.8682E-2	0.1411	3.2447E-2	0.0414	3.6708E-2	-0.0723	3.8968E-2

Table 6: Time averaged and RMS lateral forces on the rod and spacer surface using the DES model.

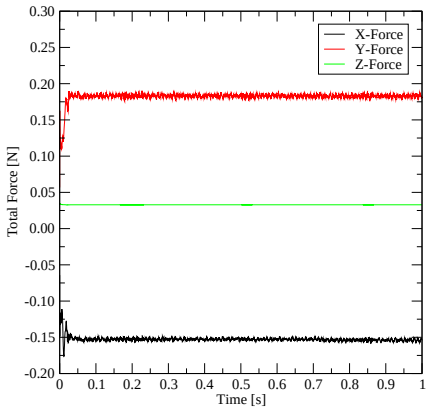

(a) Total force on the central rod.

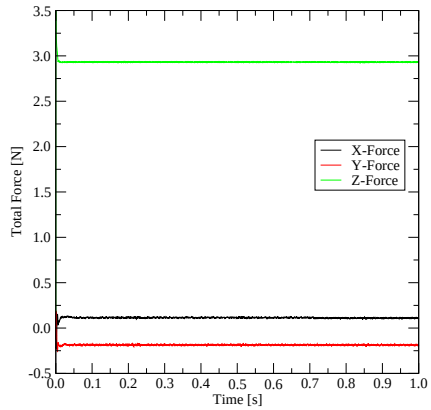

(b) Total force on the spacer.

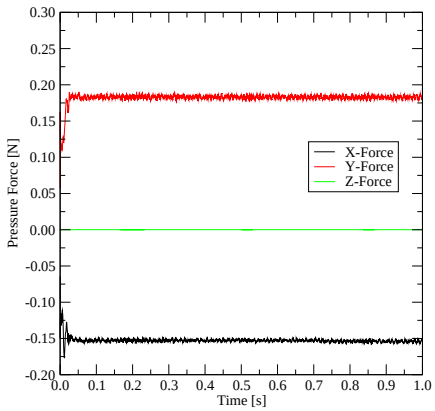

(c) Pressure force on the central rod.

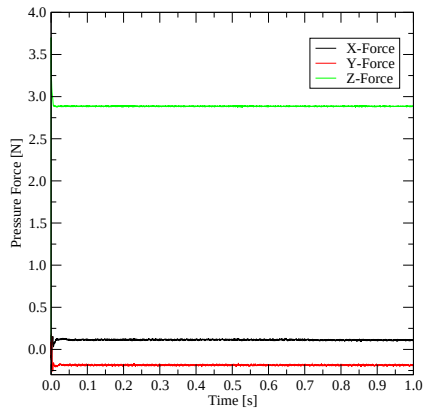

(d) Pressure force on the spacer.

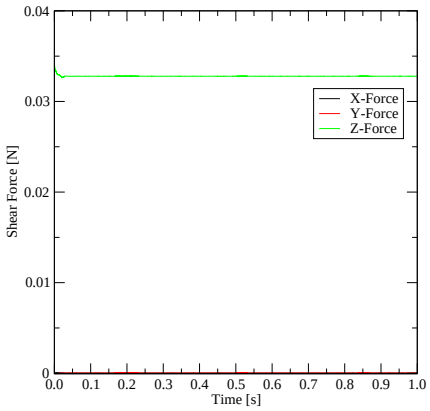

(e) Shear force on the central rod.

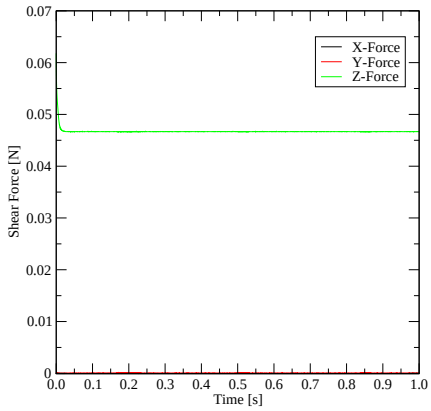

(f) Shear force on the spacer.

Figure 13: Total, pressure, and shear force time histories on the central rod and spacer for the 3M mesh using the DES model.

[h]

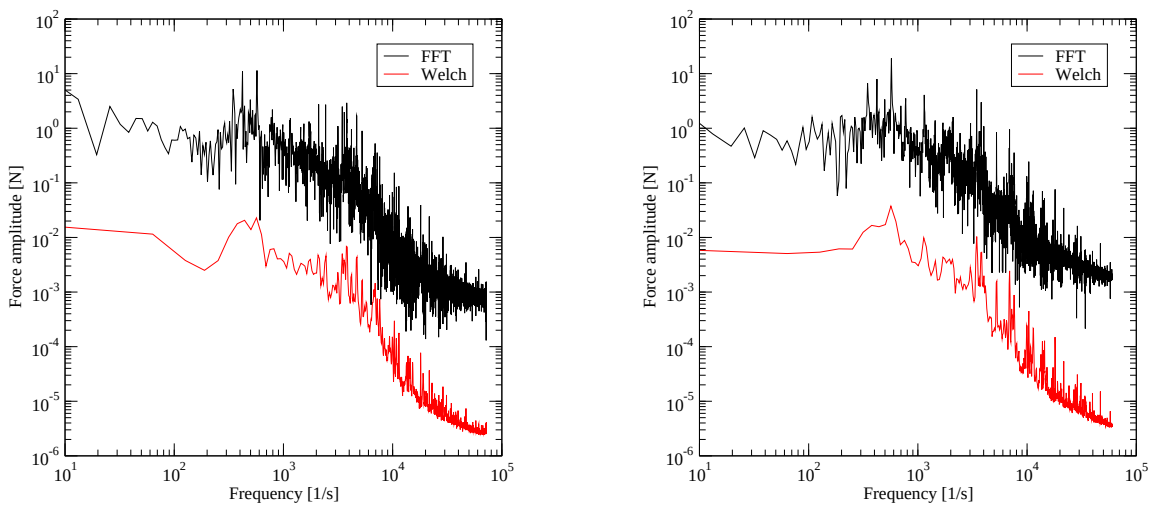

(a) FFT and Welch's PSD of the x-force.

(b) FFT and Welch's PSD of the y-force.

Figure 14: FFT and Welch's PSD of the force in the x and y directions on the central rod surface for the 3M mesh from the DES calculations.

3.2.3 Spalart-Allmaras Results

Using the Spalart-Allmaras model, we started with a fixed $CFL = 10$ for the first three meshes, in part, because we anticipated a steady-state flow solution using a RANS model on such coarse meshes. However, the persistence of localized time-dependent behavior and the fact that our stability bounds are not sharp, we were required to use $CFL = 4$ for the 6M and 12M meshes. In effect, we were testing the overall behavior of the model to assess the viability of URANS for GTRF problems.

Mesh	CFL	Avg. Time Step
672k	10	5.60E-5
1M	10	5.77E-5
3M	10	8.32E-5
6M	4	1.97E-5
12M	4	2.40E-5

Table 7: Averaged time-step based on a fixed-CFL number used for the SA calculations.

Figure 15 shows the velocity and pressure distribution at the two locations downstream of the spacer that have been presented for the ILES and DES calculations. Relative to the ILES and DES results, the vortical structures are in general smoother, the eddy sizes larger, and the low-pressures associated with the vortical structures are reduced as expected. The peak velocity magnitudes are about 28% lower than those calculated with the ILES model. In addition, the secondary eddies in the subchannels between rods are weak and barely detectable.

Helicity isosurfaces for the 3M Spalart-Allmaras calculation are shown in Figure 16. Again, the flow structures are smeared out, but still reveal significant helical structures in the flow downstream of the spacer mixing vanes. The swirl around the central rod is less pronounced, but still detectable as shown in Figure 16(b).

The kinetic energy time histories and line plots of the pressure along the surface of the central rod are shown in Figure 17. Although the kinetic energy time histories appear to indicate a perfectly steady-state solution at $t = 1$ s, there are small amplitude fluctuations. This can be seen in the force time history plots in Figure 18. The fluctuations appear to be due to small variations in the regions around the spacer where the flow is locally separated and where the resolution is fine enough for URANS with the SA model. Inspection of the time-evolution of the helicity indicated that the large helical structures, and the associated swirl, are relatively constant in time indicating a RANS behavior for the large coherent flow structures. In contrast to the ILES results, the pressure line plots shown in Figure 17(b) are relatively smooth in the section downstream of the spacer. Ultimately, the URANS calculation appears to be capturing the small oscillations around the spacer, but yielding a relatively steady RANS solution for the largest scales in the flow problem.

The cross-stream forces on the rod and spacer are shown in Figure 18. Once again, the results indicate that the forces on the rod and spacer are dominated by pressure. The shear forces on the central rod are negligibly small relative to the pressure forces. Here, the small amplitude oscillations appear to be due to the separated flow regions near the spacer and mixing vanes.

Figure 19 shows the FFT and Welch's PSD for the x and y-forces on the rod. A smoothing window size of $M = 20$ was used for the Welch PSDs. In contrast to the ILES results, there seems to be a much flatter signal over the frequency spectrum. Here, the higher-frequency

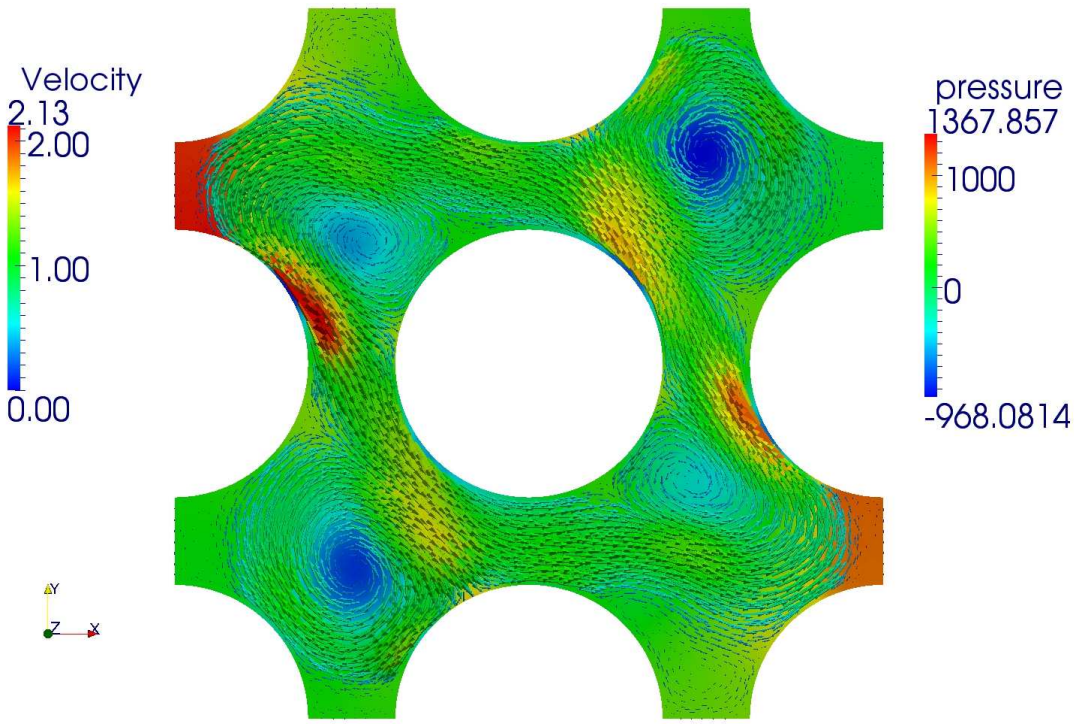

(a) Snapshot of in-plane velocity at $z = 0.1135\ m$

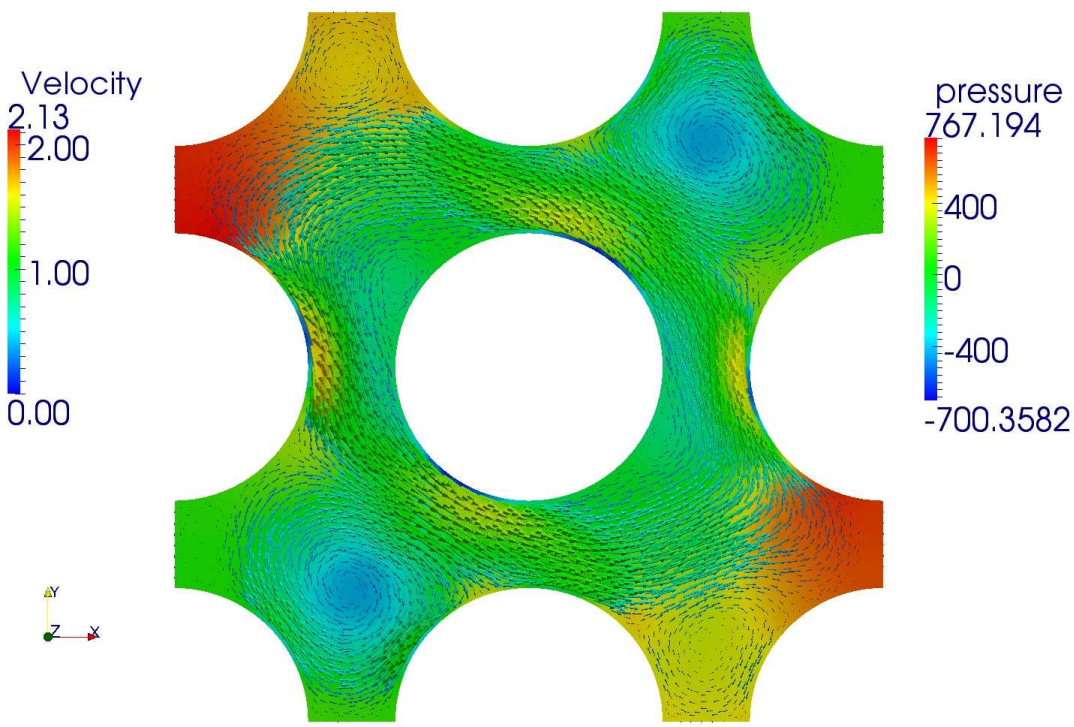

(b) Snapshot of in-plane velocity at $z = 0.1466\ m$.

Figure 15: Snapshots of velocity and pressure on cutplanes for the 3M mesh at $t = 1\ s$ using the SA model.

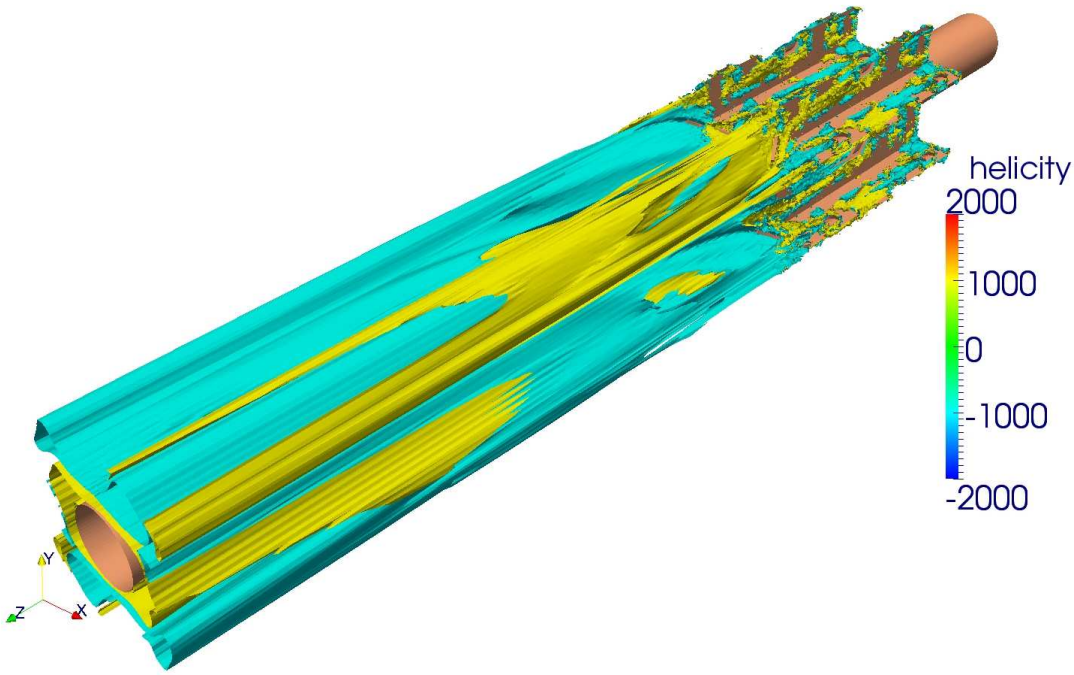

(a) Snaphost of helicity isosurfaces.

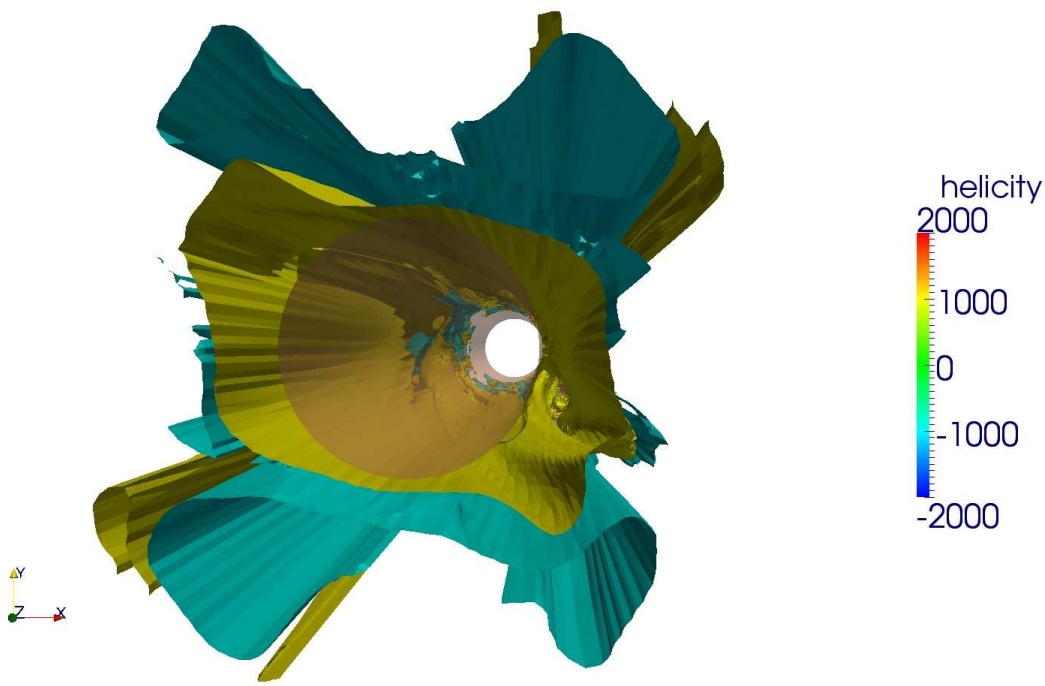

(b) Snaphost of helicity isosurfaces.

Figure 16: Instantaneous isosurfaces of helicity ($\mathbf{v} \cdot \omega$) for the 3M mesh at $t = 1$ s using the SA model. Isosurface values ± 1000 m/s^2.

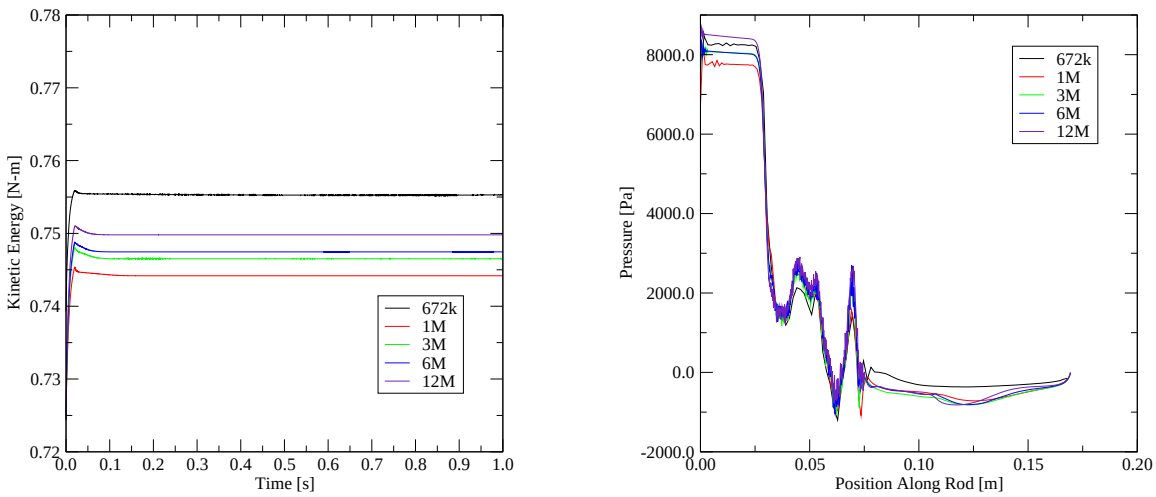

(a) Kinetic energy time history.

(b) Pressure line plots.

Figure 17: Global kinetic energy time histories, and pressure line plots for 5 meshes using the SA model.

part of the signal is likely due to small flow oscillations near the spacer. With the RANS-dominant solution with SA, it is unlikely that an accurate frequency response can be obtained for this problem and with this mesh resolution.

Making use of the force time-history data for the rod and spacer, the average and RMS forces on the rod and spacer in the cross-flow directions are reported in Table 8. The average forces are comparable to those calculated with the ILES model. However, the RMS values decrease with increasing mesh resolution. This is another indicator that the Spalart-Allmaras model is indeed trying to deliver a steady RANS solution globally.

	Rod Surface				Spacer Surface			
	X-Force		Y-Force		X-Force		Y-Force	
Mesh	Avg.	RMS	Avg.	RMS	Avg.	RMS	Avg.	RMS
672k	-0.14671	3.4903E-3	0.1036	1.6931E-3	0.0087	6.5925E-3	-0.1644	8.0364E-3
1M	-0.09263	7.3388E-4	0.1784	5.5423E-4	0.0557	3.3488E-3	-0.0789	1.4339E-3
3M	-0.13911	1.0327E-4	0.1503	8.6398E-4	0.1061	4.2756E-3	-0.2004	3.8354E-3
6M	-0.15083	4.3082E-5	0.1550	4.9546E-5	0.0224	1.6501E-4	-0.0863	1.2665E-4
12M	-0.11524	1.3817E-4	0.1326	1.7303E-4	0.0383	6.8946E-4	-0.0165	8.2192E-4

Table 8: Time averaged and RMS lateral forces on the rod and spacer surface using the SA model.

3.2.4 Pressure Drop

In this section, we discuss the measured pressure drop for the 3×3 geometry. To begin, we note that the overall pressure drop reported by Shadid, et al. [6] ranged from approximately

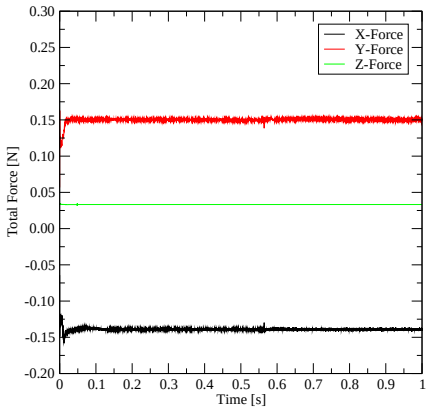

(a) Total force on the central rod.

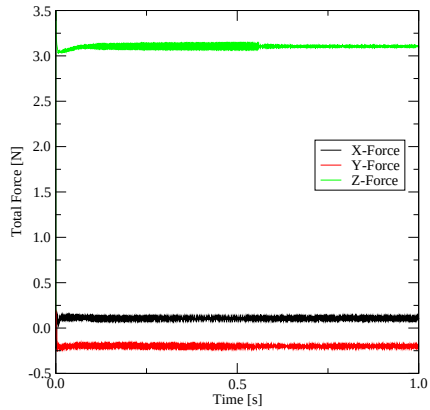

(b) Total force on the spacer.

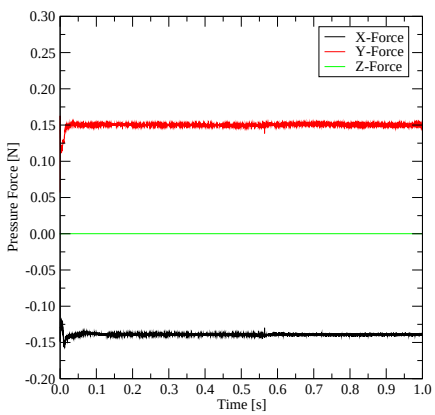

(c) Pressure force on the central rod.

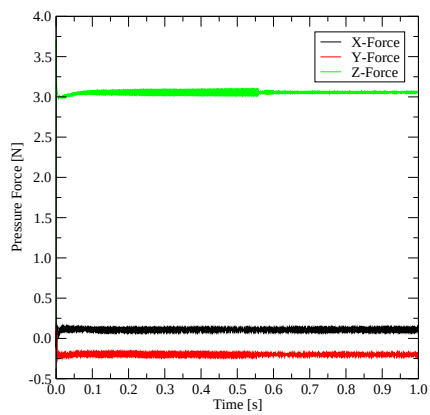

(d) Pressure force on the spacer.

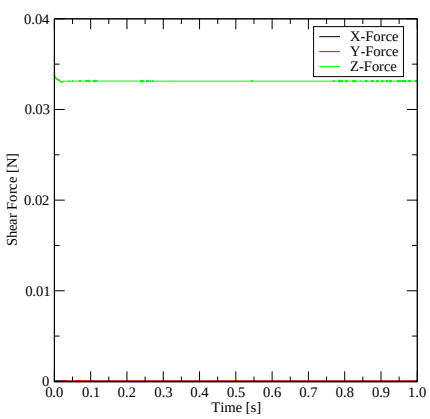

(e) Shear force on the central rod.

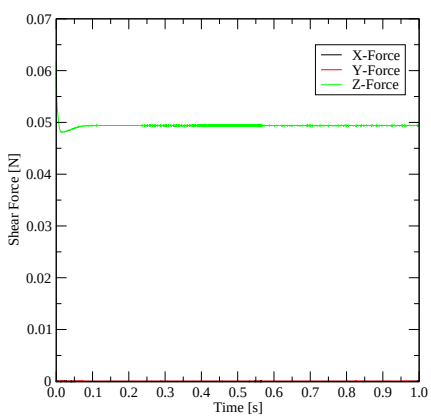

(f) Shear force on the spacer.

Figure 18: Total, pressure and shear force time histories on the central rod and spacer for the 3M mesh using the SA model.

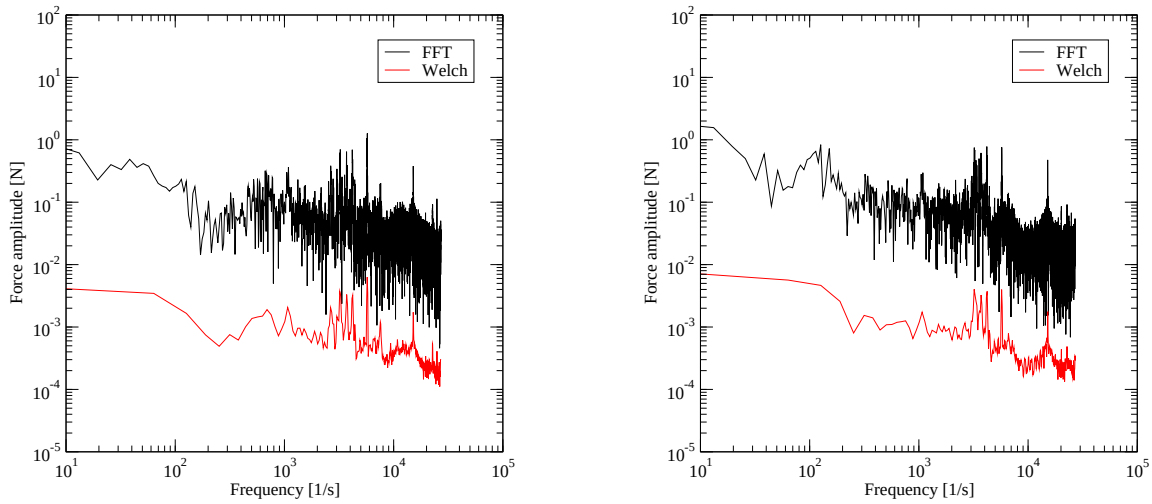

(a) FFT and Welch's PSD of the x-force.

(b) FFT and Welch's PSD of the y-force.

Figure 19: FFT and Welch's PSD of the force in the x and y directions on the central rod surface for the 3M mesh using the SA model.

24 to 27 kPa over a total length of 17.86 diameters. In contrast, the average pressure drop measured for the Elmahdi, et al. [2] problem was reported to be 15.95 kPa over 30.75 diameters [3]. For the ILES, DES and Spalart-Allmaras calculations reported here, the pressure drop over 17.86 diameters ranged from approximately 7.4 to 8.7 kPa. This data is shown in Table 9. In our work, the pressure-drop data was computed by first calculating the area-averaged inlet pressure for the rod-bundle. Time-averaging for the period $0.2 \leq t \leq 1.0$ was used to estimate the average pressure drop once the flow achieved a statistically stationary state.

The convergence rate reported by Shadid, et al. for the 1M, 3M, and 6M meshes was $p = 1.234$. Using the same 3 meshes, the ILES model yielded a convergence rate of $p = 2.067$, DES a rate of $p = 2.075$, and Spalart-Allmaras a rate of $p = 2.290$. Despite the second-order convergence rate for these three meshes, the 12M mesh shows a rapid increase in the pressure drop. Due to the non-monotonic behavior for the 3M, 6M, and 12M meshes, no attempt was made to estimate a convergence rate as the meshes are clearly still too coarse. More interesting is the fact that the local second-order convergence rate using the 1M, 3M, and 6M meshes without consideration of the velocity convergence, surface forces, etc. suggests the solution has started to converge when in fact, the 12M results show it has not.

Table 10 shows the time-averaged global kinetic energy as a function of mesh resolution for all three turbulence models considered here. Figure 20 shows the pressure drop and kinetic energy as a function of the mesh resolution. As previously reported by Shadid, et al. [6], the convergence of the pressure is non-monotonic suggesting that the 672k mesh is simply too coarse. This effect is also pronounced in the kinetic energy variation with mesh resolution. Although the kinetic energy appears to be starting to asymptote to a constant value for the ILES model, the pressure drop, an integral quantity, does not exhibit the same trend suggesting that the meshes may be too coarse for a systematic convergence study.

Mesh	ILES Δp $[Pa]$	DES Δp $[Pa]$	SA Δp $[Pa]$
672k	7766.2	7974.1	8623.0
1M	7362.0	7443.1	7917.1
3M	7799.1	7812.9	8287.1
6M	7860.6	7864.5	8329.7
12M	8350.4	8398.9	8691.0

Table 9: Pressure drop for the GTRF meshes with ILES, DES, and SA models. The pressure drop, Δp, here is computed as the difference between the (spatially and temporally averaged, $0.2 \leq t \leq 1.0$) pressure at the inflow and the outflow pressure prescribed as zero. The data are plotted in Figure 20(a).

Mesh	ILES KE $[N-m]$	DES KE $[N-m]$	SA KE $[N-m]$
672k	0.7624	0.7578	0.7553
1M	0.7595	0.7522	0.7442
3M	0.7665	0.7589	0.7465
6M	0.7720	0.7647	0.7475
12M	0.7748	0.7729	0.7498

Table 10: Temporally, $0.2 \leq t \leq 1.0$, and domain-averaged kinetic energy for the GTRF meshes with ILES, DES, and SA models. The data are plotted in Figure 20(b).

However, using the time-averaged kinetic energy for the ILES model, the convergence rate observed using the 3M, 6M and 12M meshes is

$$KE = 0.7779 - 0.01142 \left(\frac{h}{h_c}\right)^{2.5155} \tag{2}$$

where h/h_c is the ratio of the current to coarsest mesh spacing. Here, we assume that $h/h_c = (Nel/Nel_c)^{1/3}$, where, Nel is the number of elements in the mesh, and Nel_c is the number of elements for the coarsest mesh, i.e., the 3M mesh.

We note in passing that the estimation of the convergence rate and asymptotic value (as $h \to 0$) are sensitive to the estimate for h. In reproducing the Eq. (18) in Rider [5], we noticed that small perturbations in the estimation of h yielded large variations in the asymptotic value and the convergence rate. Given the non-monotonic behavior of the pressure for the 3M, 6M and 12M meshes, we did not estimate convergence rates for the DES and Spalart-Allmaras results.

Given the differences between the Hydra-TH, Drekar and CCM+ pressure drop estimates, we investigated the differences and the potential causes. Assuming that the Star-CCM+ results computed on a 48 million element mesh are reasonably accurate, we computed an overall pressure loss coefficient using the Darcy-Weisbach formula. This assumes the pressure drop is uniformly distributed over the length of the domain. Using the pressure drop coefficient with the $17.86d$ length of the 3×3 array, the pressure drop is approximately 9.27 kPa. This is a suggestive, but not a conclusive result, given the localized pressure drop around the spacer (see for example, Figure 7(b)), and so we have conducted a series of additional tests to try and understand the differences between reported pressure drops for the 3×3 geometry.

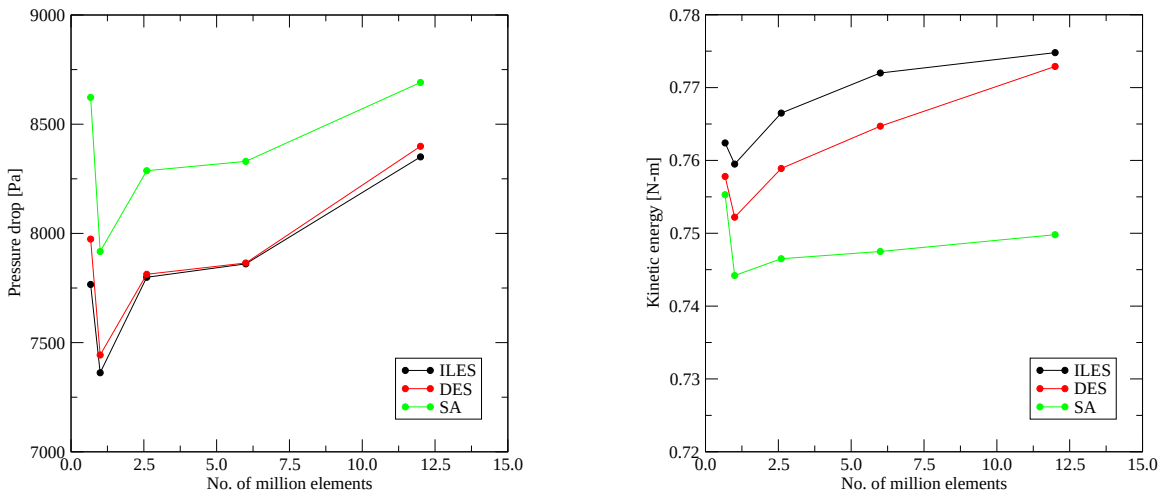

(a) Pressure drop convergence.

(b) Averaged kinetic energy convergence.

Figure 20: Mesh convergence of the pressure drop and averaged kinetic energy for the GTRF meshes with ILES, DES, and SA models.

First, we have generated an independent "checkout" problem using Poiseuille flow as a double-check that our pressure-gradient correctly balances the viscous forces for a simple laminar analytical case. Here, a $Re = 100$ Poiseuille flow was used with a $20 \times 1 \times 1$ domain. The calculation was run until a steady-state was achieved. The pressure drop was measured over 9 m between $x = 10$ and $x = 19$ m. Figure 21(a) shows the velocity and pressure distributions for the overall domain. Figure 21(b) shows the parabolic velocity profile at $x = 10$ and $x = 19$. The velocity profiles are identical indicating that a hydrodynamically fully-developed flow has been established. Using the peak velocity value measured in the code, and the analytic relationship for Poiseuille flow, the analytic pressure gradient matches the calculated gradient measured for $10 \leq x \leq 19$ m. This suggests that at least there is not an egregious bug that is resulting in pressure drops significantly lower than reported for Drekar in [6].

Since our calculations used a no-penetration/slip condition at the edges of the subchannels, we replaced the no-penetration boundary conditions with prescribed velocities with a magnitude of $0.1m/s$ that emulate a net cross-flow in the x and y-directions. This increased the overall pressure drop to approximately 9 kPa. Unfortunately, this does not explain the overall $3\times$ difference in the pressure drop.

We also conducted a series of calculations increasing the molecular viscosity from a factor of 3 to 25 times the molecular viscosity of 2.32×10^{-4} $kg/m/s$ used in the Hydra-TH calculations and reported by Shadid, et al. [6]. A continuous increase in overall pressure drop was observed as expected. For a viscosity that is factor 25 times larger, the overall pressure drop was approximately 24 kPa. Although this series of tests is suggestive, without a more detailed investigation, we can only speculate as to the potential causes of the difference in pressure drop observed between Hydra-TH, CCM+ and Drekar.

Finally, we note that all of the computed results with Hydra-TH indicated the presence

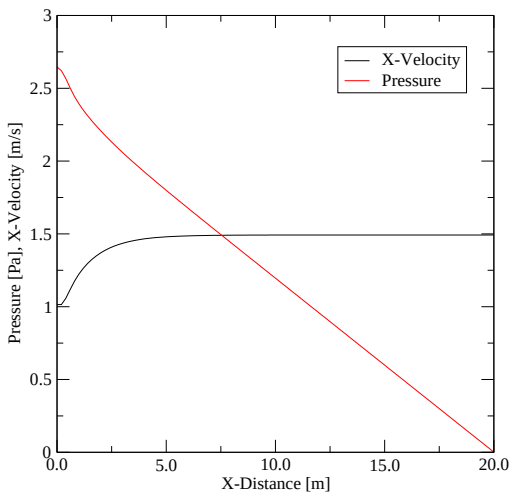

(a) Pressure and velocity profiles.

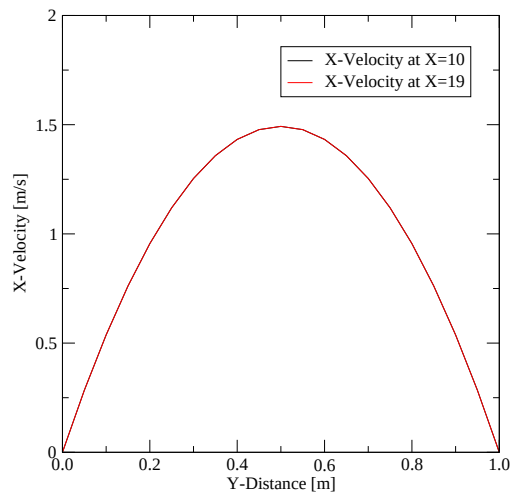

(b) Velocity profile at two locations along the flow axis.

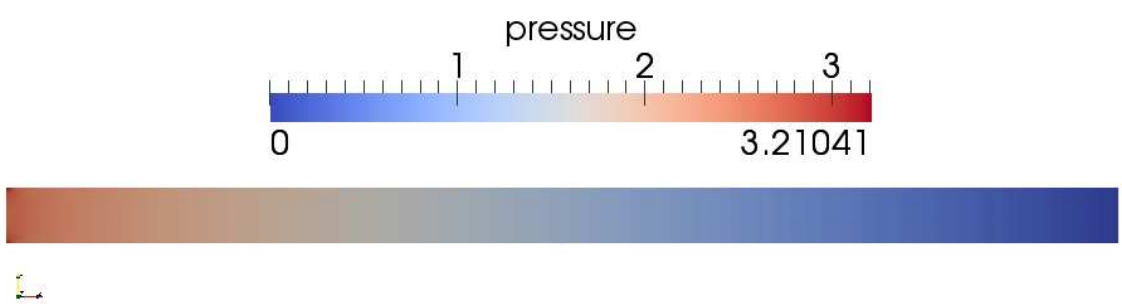

(c) Pressure distribution.

Figure 21: Poiseuille flow test.

of relatively strong vortical structures that persist downstream of the spacer. These vortical structures persist at the outflow boundary indicating a mismatch between the local pressure at the vortex core, and the outflow condition that sets the hydrostatic pressure. This suggests that the boundary is too close to the spacer, and that either the domain should be longer, or alternative outflow boundary conditions applied. A longer flow domain such as the 30.75 diameter long domain used by Elmahdi, et al. with CCM+ may be sufficiently long.

3.3 Spider Meshes (Task-4)

The Hydra-TH team has worked with Greg Sjaardema at Sandia National Laboratories to test the scalability of the Exodus-II library in the billion element range. At this point, we have successfully used the netcdf4/HDF5 Exodus-II library with a small utility code to generate a 1.8 billion element channel mesh and store it in an Exodus-II file. This utility code and the netcdf4, HDF5 and Exodus-II libraries have been provided to Numeca for integration into the Hexpress/Hybrid mesh generator. The same utility code and libraries have also been provided to CD-Adapco for development of a CCM+ to Exodus-II translator.

At this time, we have just received our license for Hexpress/Hybrid which will permit us to generate large hybrid meshes. Numeca has completed integration of the Exodus-II/netcdf4/HDF5 libraries, and will deliver an incremental release in the near future. They have also provided initial test meshes in Exodus-II format that we have tested and successfully visualized in ParaView. We will begin evaluation calculations using hybrid meshes from Hexpress/Hybrid with Hydra-TH as soon as practically possible.

3.4 Supporting Work

During the course of executing the milestone tasks, a number of related and supporting tasks have been carried out by the Hydra-TH team. As a part of Task-4, we have made improvements in the Hydra-TH I/O to permit reading and writing HDF5-based Exodus-II files. This effort yielded significant speedups relative to the older version of Exodus-II, in addition to having the capability to handle grids up to 2.1 billion cells. Testing with the HDF5-based Exodus-II files has demonstrated a factor of 40 speedup for small problems, and a factor of 6.8 speedup on larger problems.

As part of carrying out the milestone calculations, output delegates for surface field and time history output has been implemented in Hydra-TH. This activates a rich suite of user selectable output that includes data such as surface heat flux, normal heat flux, tractions, shear forces, y^+, y^*, etc. In addition, this effort has activated history output for both surface history data (e.g., integral flow quantities, average pressure, temperature, etc.), as well as point-wise time history data.

An initial port of Hydra-TH to Jaguar XK5 has been completed so that we could carry out some of the milestone calculations using Jaguar using thousands of cores. We are starting to exercise Hydra-TH regularly on Jaguar and plan additional scaling studies in the near future. To support this, we have extended our load balancing interface to include recursive coordinate bisection (RCB) and recursive inertial bisection (RIB) algorithms that are more amenable to the structured channel mesh problem reported in milestone report THM.CFD.P3.02 [1]. At the time of this writing, we have just completed a port to the XK6 partition of Jaguar, and are beginning a scaling study.

During the milestone activities, we have worked closely with David DeMarle and Berk Geveci at Kitware on distance visualization for our Jaguar calculations, and to make sure

that the HDF5 based Exodus-II files are supported by ParaView. At this time, we are able to visualize relatively large datasets remotely using parallel distributed files, and hope to scale up both problem size and number of processors in the very near term.

4 Summary and Future Directions

A series of tasks have been carried out as defined by the Hydra-TH L2 Milestone (THM.CFD.P4.01). Task 3 was conditional and omitted from this report. A series of computations on the GTRF meshes delivered from Sandia have been carried out using Hydra-TH and three different turbulence models (ILES, DES, SA). A preliminary investigation indicated that all calculations should be carried out to approximately 1 s in order to achieve a statistically stationary state for the ILES, DES, and SA models. In general, the overall mesh quality is relatively poor for LES calculations with relatively poorly resolved boundary layers and rapid jumps in mesh resolution. In effect, the ILES and DES calculations are essentially very large-eddy simulation, or more simply "dirty LES".

A qualitative comparison between the velocity distributions computed by Elmahdi, et al. [2] show reasonable agreement in terms of the vortical structure and in-plane velocity magnitude. However, pressure drop comparisons between Hydra-TH, Drekar and the CCM+ results of Elmahdi, et al. leave a number of unanswered questions. The presence of relatively strong vortical motion at the outflow boundary suggests that this boundary is too close to the spacer, or that alternative boundary conditions are required for this domain.

The results presented for the ILES, DES and Spalart-Allmaras turbulence models in §3.2.1 – 3.2.3 indicates a number of differences in the computed results. This is not surprising given the nature of turbulence and the approaches to turbulence modeling. Despite using a time-accurate URANS approach with Spalart-Allmaras, the time-history force data suggest that this approach may not be a viable approach for GTRF calculations where the mean and RMS forces are of interest. However further studies with refined meshes and better boundary layer mesh grading are required to make a definitive statement. In addition, it may be worthwhile to investigate some level of turbulent statistics rather than only considering mean and RMS values of forces. In terms of design processes, it is anticipated that there are a number of loading and heat transfer metrics that would be useful in determining the "best" turbulence model for GTRF and ultimately an optimal spacer design. However, these metrics are not currently available, and a discussion of this topic is beyond the scope of this report.

In addition to the primary tasks for the milestone, a series of important steps were carried out as supporting work. This includes the scaling of the HDF5-based Exodus-II library to 1.8 billion cells. In addition, the Hydra-TH team has work closely with Kitware to debug distance visualization between ORNL and LANL using Jaguar. In addition, we have worked with Numeca on the integration of the Exodus-II, netcfd4, and HDF5 libraries into Hexpress/Hybrid. We are beginning a more serious use and evaluation of Hexpress/Hybrid for CASL-centric THM problems.

In the process of porting Hydra-TH to Jaguar, we encountered a number of issues that we have resolved with the help of the NCCS consultants. These have included

1. *Invalid MPI tags.* Appearing only on core counts between 2048 and 5000, Cray's MPICH generates fatal errors during MPI sends: `aborting job: Fatal error in MPI_Isend: Invalid tag`.

2. *Dropped EQ handle.* Also appearing only on core counts in the thousands, another Cray-specific communication error is `MPICH PtlEQPoll error PTL_EQ_DROPPED`.

3. Exceeding the MPI tag size which is limited to a 23-bit representation.

As we move forward with Hydra-TH, we are planning a series of additional steps relevant to the GTRF problem.

- Perform a more detailed scaling study on Jaguar using meshes up to ≈ 1 billion elements
- Implement the WALE model [4] to be consistent with Star-CCM+ and Drekar
- Extend the implementation of time-averaging and turbulence statistics calculations for large GTRF models
- Investigate the use of hybrid "Spider" meshes for the GTRF problem
- Perform a more detailed comparison of turbulence models using more refined meshes with more appropriate boundary layer resolution. These studies should make use of the 30.75 diameter long 3×3 and provide better data for pressure drop comparisons.

We believe these to be necessary first steps in addressing some of the issues identified in this report.

ACKNOWLEDGMENTS

The authors would like to thank Ramanan Sankaran at Oak Ridge National Laboratory for his help with porting issues on Jaguar, and Greg Sjaardema at Sandia National Laboratories for his help with scaling up the Exodus-II/netcdf4/HDF5 libraries. We also acknowledge the help we've received from David DeMarle and Berk Geveci at Kitware for their help with ParaView and distance visualization.

References

[1] M. A. Christon, *Hydra-TH Theory Manual*, Tech. Rep. LA-UR 11-05387, Los Alamos National Laboratory, September 2011.

[2] A. M. Elmahdi, R. Lu, M. E. Conner, Z. Karoutas, and E. Baglietto, *Flow induced vibration forces on a fuel rod by les cfd analysis*, in The 14th International Topical Meeting on Nuclear Reactor Thermal Hydraulics (NURETH-14), Hilton Toronto Hotel, Toronto, Ontario, Canada, September 2011.

[3] A. Mandour, *Personal communication.* December 2011.

[4] F. Nicoud and F. Ducros, *Subgrid-scale stress modelling based on the square of the velocity gradient tensor*, Flow, Turbulence and Combustion, 62 (1999), pp. 183–200. 10.1023/A:1009995426001.

[5] W. J. Rider, *Solution verification applied to Drekar and Fuego calculations using of grid-to-rod-fretting (gtrf)*, tech. rep., Sandia National Laboratories, 2011.

[6] J. N. Shadid, T. M. Smith, R. P. Pawlowski, E. C. Cyr, P. D. Weber, and D. Z. Turner, *Initial drekar LES CFD simulations for grid-torod fretting (gtrf) (thm.cfd.p2.01)*, tech. rep., Sandia National Laboratories, 2011.

[7] P. Welch, *The use of fast fourier transform for the estimation of power spectra: A method based on time averaging over short, modified periodograms*, Audio and Electroacoustics, IEEE Transactions on, 15 (1967), pp. 70–73.